

# Evidence for past interaction with an asymmetric circumstellar shell in the young SNR Cassiopeia A

S. Orlando<sup>1</sup>, A. Wongwathanarat<sup>2</sup>, H.-T. Janka<sup>2</sup>, M. Miceli<sup>3,1</sup>, S. Nagataki<sup>4,5</sup>, M. Ono<sup>4,5</sup>,  
F. Bocchino<sup>1</sup>, J. Vink<sup>6,7,8</sup>, D. Milisavljevic<sup>9</sup>, D.J. Patnaude<sup>10</sup>, and G. Peres<sup>3,1</sup>

<sup>1</sup> INAF – Osservatorio Astronomico di Palermo, Piazza del Parlamento 1, I-90134 Palermo, Italy  
e-mail: salvatore.orlando@inaf.it

<sup>2</sup> Max-Planck-Institut für Astrophysik, Karl-Schwarzschild-Str. 1, D-85748 Garching, Germany

<sup>3</sup> Dip. di Fisica e Chimica, Università degli Studi di Palermo, Piazza del Parlamento 1, 90134 Palermo, Italy

<sup>4</sup> Astrophysical Big Bang Laboratory, RIKEN Cluster for Pioneering Research, 2-1 Hirosawa, Wako, Saitama 351-0198, Japan

<sup>5</sup> RIKEN Interdisciplinary Theoretical & Mathematical Science Program (iTHEMS), 2-1 Hirosawa, Wako, Saitama 351-0198, Japan

<sup>6</sup> Anton Pannekoek Institute for Astronomy, University of Amsterdam, Science Park 904, 1098 XH Amsterdam, The Netherlands

<sup>7</sup> GRAPPA, University of Amsterdam, Science Park 904, 1098 XH Amsterdam, The Netherlands

<sup>8</sup> SRON, Netherlands Institute for Space Research, Utrecht, The Netherlands

<sup>9</sup> Department of Physics and Astronomy, Purdue University, 525 Northwestern Avenue, West Lafayette, IN 47907, USA

<sup>10</sup> Smithsonian Astrophysical Observatory, 60 Garden Street, Cambridge, MA 02138, USA

Received date / Accepted date

## ABSTRACT

**Context.** Observations of the supernova remnant (SNR) Cassiopeia A (Cas A) show significant asymmetries in the reverse shock that cannot be explained by models describing a remnant expanding through a spherically symmetric wind of the progenitor star.

**Aims.** We investigate whether a past interaction of Cas A with a massive asymmetric shell of the circumstellar medium can account for the observed asymmetries of the reverse shock.

**Methods.** We performed three-dimensional (3D) (magneto)-hydrodynamic simulations that describe the remnant evolution from the SN explosion to its interaction with a massive circumstellar shell. The initial conditions (soon after the shock breakout at the stellar surface) are provided by a 3D neutrino-driven SN model whose morphology closely resembles Cas A (Wongwathanarat et al. 2017) and the SNR simulations cover  $\approx 2000$  years of evolution. We explored the parameter space of the shell, searching for a set of parameters able to produce an inward-moving reverse shock in the western hemisphere of the remnant at the age of  $\approx 350$  years, analogous to that observed in Cas A.

**Results.** The interaction of the remnant with the shell can produce asymmetries resembling those observed in the reverse shock if the shell was asymmetric with the densest portion in the (blueshifted) nearside to the northwest (NW). According to our favorite model, the shell was thin (thickness  $\sigma \approx 0.02$  pc) with a radius  $r_{\text{sh}} \approx 1.5$  pc from the center of the explosion. The reverse shock shows the following asymmetries at the age of Cas A: i) it moves inward in the observer frame in the NW region, while it moves outward in most other regions; ii) the geometric center of the reverse shock is offset to the NW by  $\approx 0.1$  pc from the geometric center of the forward shock; iii) the reverse shock in the NW region has enhanced nonthermal emission because, there, the ejecta enter the reverse shock with a higher relative velocity (between 4000 and 7000 km s<sup>-1</sup>) than in other regions (below 2000 km s<sup>-1</sup>).

**Conclusions.** The large-scale asymmetries observed in the reverse shock of Cas A can be interpreted as signatures of the interaction of the remnant with an asymmetric dense circumstellar shell that occurred between  $\approx 180$  and  $\approx 240$  years after the SN event. We suggest that the shell was, most likely, the result of a massive eruption from the progenitor star that occurred between  $10^4$  and  $10^5$  years prior to core-collapse. We estimate a total mass of the shell of the order of  $2 M_{\odot}$ .

**Key words.** hydrodynamics – instabilities – shock waves – ISM: supernova remnants – X-rays: ISM – supernovae: individual (Cassiopeia A)

## 1. Introduction

Cassiopeia A (in the following Cas A) is one of the best studied supernova remnants (SNRs) of our Galaxy. Its relative youth (with an age of  $\approx 350$  years; Fesen et al. 2006) and proximity (at a distance of  $\approx 3.4$  kpc; Reed et al. 1995) make this remnant an ideal target to study the structure and chemical composition of the stellar material ejected by a supernova (SN). The analysis of multi-wavelength observations allowed some authors to reconstruct in great details its three-dimensional (3D) structure (e.g., DeLaney et al. 2010; Milisavljevic & Fesen 2013, 2015; Grefenstette et al. 2014, 2017). Several lines of evidence suggest

that the morphology and expansion rate of Cas A are consistent with a remnant mainly expanding through a spherically symmetric wind of the progenitor star (e.g., Lee et al. 2014). Thus, the vast majority of anisotropies observed in the remnant morphology most likely reflect asymmetries left from the earliest phases of the SN explosion. This makes Cas A a very attractive laboratory to link the physical, chemical and morphological properties of a SNR to the processes at work during the complex phases of the SN.

First attempts to link Cas A to its parent SN were very successful and have shown that the bulk of asymmetries observed in the remnant are intrinsic to the explosion (Orlando et al. 2016), and the extended shock-heated Fe-rich regions evident in the

Send offprint requests to: S. Orlando

main shell originate from large-scale asymmetries that developed from stochastic processes (e.g., convective overturn and the standing accretion shock instability; SASI) during the first seconds of the SN blast wave (Wongwathanarat et al. 2017). More recently, Orlando et al. (2021) (in the following Paper I) have extended the evolution of the neutrino-driven core-collapse SN presented in Wongwathanarat et al. (2017) till the age of 2000 years with the aim to explore how and to which extent the remnant keeps memory of post-explosion anisotropies imprinted to the ejecta by the asymmetric explosion mechanism. Comparing the model results for the SNR at  $\approx 350$  years with observations shows that the main asymmetries and features observed in the ejecta distribution of Cas A result from the interaction of the post-explosion large-scale anisotropies in the ejecta with the reverse shock.

The above models, however, do not explain one of the most intriguing aspects of the Cas A structure, as evidenced by the analysis of the position and velocity of the forward and reverse shocks. Observations in different wavelength bands indicate a forward shock expanding with a velocity around  $\approx 5500 \text{ km s}^{-1}$  along the whole remnant outline (e.g., DeLaney & Rudnick 2003; Patnaude & Fesen 2009; Fesen et al. 2019; Vink et al. 2022) and a reverse shock moving outward with velocity ranging between  $2000 \text{ km s}^{-1}$  and  $4000 \text{ km s}^{-1}$  in the eastern and northern hemisphere of the remnant (e.g., Sato et al. 2018; Fesen et al. 2019; Vink et al. 2022). These velocities are somehow consistent with the remnant expanding through a spherically symmetric wind of the progenitor star and, in fact, are well reproduced by the models (e.g., Orlando et al. 2016 and Paper I). The observations, however, suggest that the reverse shock in the southern and western quadrants of Cas A is stationary or is even moving inward in the observer frame toward the center of the explosion (e.g., Anderson & Rudnick 1995; Keohane et al. 1996; DeLaney et al. 2004; Morse et al. 2004; Helder & Vink 2008; Sato et al. 2018) at odds with the model predictions (e.g., Vink 2020; Vink et al. 2022; see also Paper I). In addition, observations of Cas A show an offset of  $\approx 0.2 \text{ pc}$  (at the distance of  $3.4 \text{ kpc}$ ) between the geometric center of the reverse shock and that of forward shock (Gotthelf et al. 2001) that cannot be reproduced by the models (see Paper I).

The above results are even more puzzling by looking at the X-ray synchrotron emission associated with the forward and reverse shocks. Helder & Vink (2008) have shown that the reverse shock radiation is limited to a thin spherical shell partially visible mainly in the western hemisphere and shifted toward the west with respect to the remnant outline (thus again suggesting an offset between the centers of the reverse and forward shocks). A similar conclusion was reached by analyzing radio observations of Cas A (see upper panel of Fig. 1), which show that the forward and reverse shocks are much closer to each other and the radio emission is higher in the western than in the eastern hemisphere (Arias et al. 2018). Helder & Vink (2008) have proposed that the high synchrotron emission in the western hemisphere is due to a locally higher reverse shock velocity in the ejecta rest frame ( $\approx 6000 \text{ km s}^{-1}$ ), so that, there, the reverse shock is able to accelerate electrons to the energies needed to emit X-ray synchrotron radiation (see lower panel of Fig. 1).

Some hints about the possible cause of the unexpected reverse shock dynamics come from the evidence that isolated knots of ejecta show a significant blue and redshift velocity asymmetry: ejecta traveling toward the observer have, on average, lower velocities than ejecta traveling away (e.g., Reed et al. 1995; DeLaney et al. 2010; Milisavljevic & Fesen 2013). It is debated as to whether this is due to the explo-

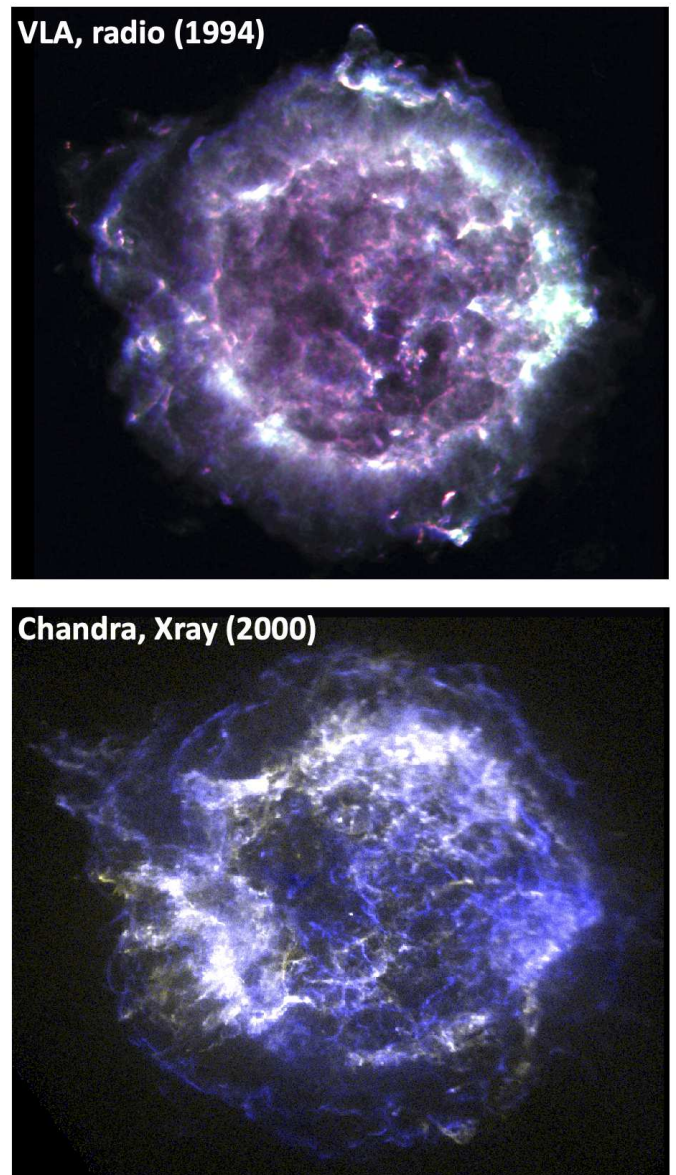


**FIG. 1:** Upper panel: radio observation of Cas A collected with the Very Large Array telescope in 1994 at the frequencies 1.4 GHz (L band), 5.0 GHz (C band) and 8.4 GHz (X band), which highlights the emission dominated by synchrotron radiation (Credit: L. Rudnick, T. Delaney, J. Keohane, B. Koralesky and T. Rector; NRAO/AUI/NSF). Lower panel: X-ray observation of Cas A collected with Chandra in 2000, in sqrt scale, showing the emission in the [0.5, 2] keV (white) and [2, 7] keV (blue) bands.

sion dynamics (DeLaney et al. 2010; Isensee et al. 2010) or expansion into inhomogeneous circumstellar medium (CSM; Reed et al. 1995; Milisavljevic & Fesen 2013). Observations of slow-moving shocked circumstellar clumps in the remnant, the so-called “quasi-stationary flocculi” (QSFs), seem to favor the latter scenario. In fact, these structures are, in large majority, at blue shifted velocities (Reed et al. 1995), implying that more CSM material is placed in the front than in the back of Cas A. This may suggest that the asymmetries associated with the velocities of ejecta knots and, most likely, the evidently asymmetric structure of the reverse shock in Cas A may reflect the in-

teraction of the remnant with an inhomogeneous structure of the CSM.

Further support to the scenario of inhomogeneous CSM comes from radio and X-ray observations which suggest that the remnant is interacting with a density jump in the ambient medium (probably a local molecular cloud) in the western hemisphere (Keohane et al. 1996; Sanders 2006; Hwang & Laming 2012; Kilpatrick et al. 2014). More recently, Sato et al. (2018) have analyzed Chandra and NuSTAR observations of Cas A (see lower panel of Fig. 1), identifying inward-moving shocks in the observer frame located from a region close to the compact central object (inside the mean reverse shock radius derived by Gotthelf et al. 2001) to the maximum of the dense shell brightness to the west (coincident with the reverse-shock circle). The authors connected these shocks with the brightest features in X-ray synchrotron radiation seen with NuSTAR. Since in spherical symmetry, an inward-moving reverse shock is not consistent with the dynamical age of a SNR as young as Cas A, they proposed that the inward moving shocks are reflected shocks caused by the interaction of the blast wave with a molecular cloud with a density jump  $> 5$ .

The possibility that the remnant is interacting with molecular clouds is reasonable and may explain some of the features of the reverse shock (e.g., Kilpatrick et al. 2014; Sato et al. 2018). This interaction would imply a deceleration of the forward shock that propagates through a denser medium and, possibly, an indentation in the remnant outline (e.g., Slane et al. 2015). However, both of these signatures of interaction are not clearly visible in Cas A: the forward shock shows similar velocities along the remnant outline and both the forward and reverse shocks have shapes that are roughly spherical, without any sign of interaction with a molecular cloud. Furthermore, most of the molecular gas detected lies in the foreground of Cas A (e.g., Krause et al. 2004; Wilson & Batrla 2005; Dunne et al. 2009; Koo et al. 2018) and would not have any effect on the propagation of the forward and reverse shocks.

If, on one hand, an ongoing interaction of the remnant with a molecular cloud seems not to be plausible to justify the asymmetries observed in the reverse shock of Cas A, it is possible, on the other hand, that the remnant has encountered a dense shell of the CSM in the past (e.g., Borkowski et al. 1996) and the signatures of that interaction are now visible in the structure of the reverse shock. In fact, massive stars are known to experience episodic and intense mass loss events before going to SN. These events may be related, for instance, with the activity of luminous blue variable stars (LBVs; Conti 1984) and Wolf-Rayet stars (WR stars; Foley et al. 2007; Pastorello et al. 2007, 2008; Smith et al. 2020). In these cases, after the explosion, the shock wave from the SN travels through the wind of the progenitor and, at some point, collides with the material of pre-SN mass loss events (see Smith 2014 for a recent review). For instance, strong indications of interaction with a circumstellar shell, likely associated with wind residual, have been recently found in the Vela SNR (Sapienza et al. 2021).

Observations of light echoes showed that Cas A is the remnant of a Type IIb SN (Krause et al. 2008; Rest et al. 2011). This implies that its progenitor star has shed almost all of its H envelope (see also Kamper & van den Bergh 1976; Chevalier & Kirshner 1978) before the core-collapse. Various hypotheses have been proposed to explain how the progenitor star of Cas A has lost its envelope: via its own stellar wind (e.g., Heger et al. 2003), or via binary interaction that involves mass transfer and, possibly, a common-envelope phase (e.g., Podsiadlowski et al. 1992), or via interaction of the pro-

genitor with the first SN of a binary that removed its envelope (Hirai et al. 2020). In any case, the expanding remnant, at some point, should have encountered and interacted with the gas of these pre-SN mass loss events. In an early study, Chevalier & Liang (1989) have suggested that Cas A interacted with a circumstellar shell in the past and identified its bright ring with the shocked shell. A few years later, this idea was further investigated by Borkowski et al. (1996) through a 1D numerical model. These authors have proposed that the blast wave of Cas A traveled through an inhomogeneous CSM characterized by a circumstellar shell resulted from the interaction of the slow stellar wind in the red supergiant stage of the progenitor star with the faster wind in the subsequent blue supergiant stage. Koo et al. (2018) have interpreted the spatial distribution of QSFs observed in Cas A as evidence of a massive eruption from the progenitor system to the west, which most likely occurred  $10^4 - 10^5$  years before the SN. Observations of the circumstellar environment around Cas A have also shown evidence of nebulosities that have been interpreted to be the relics of the red supergiant mass-loss material from Cas A's progenitor (Weil et al. 2020).

Here, we investigate whether some of the large-scale asymmetries in the reverse shock of Cas A may reflect the past interaction of the remnant with a dense shell of CSM, most likely the consequence of an episodic mass loss from the progenitor massive star that occurred in the latest phases of its evolution before collapse. To this end, we reconsidered our model for describing the remnant of a neutrino-driven core-collapse SN that reproduces the main features of Cas A (presented in Paper I), but added the description of an asymmetric shell of CSM with which the remnant interacts within the first 300 years of evolution. We performed an extensive simulation campaign to explore the parameter space of the shell and derived, from the models, the profiles of the forward and reverse shock velocity versus the position angle in the plane of the sky at the age of Cas A. By comparing the profiles derived from the models with those inferred from the observations (Vink et al. 2022) we identified the models which better than others reproduce the observations. Since no complete survey of parameter space can possibly be done, we do not expect an accurate match between models and observations and we cannot exclude that shells with structure different from those explored here can do a better job in matching the observations.

Indeed, we do not aim at deriving an accurate, unique, description of the CSM. Our idealized shell model aims at showing that the main large-scale asymmetries observed in the reverse shock of Cas A (namely, the inward-moving reverse shock observed in the western hemisphere, the offset between the geometric centers of the reverse and forward shocks, and the evidence that the nonthermal emission from the reverse shock is brighter in the western than in the eastern region) can be naturally explained as the result of a past interaction of the remnant with a circumstellar shell. The study is also relevant for disentangling the effects from interior inhomogeneities and asymmetries (produced soon after the core-collapse) from those produced by the interaction of the remnant with an inhomogeneous CSM. Future studies are expected to consider a structure of the CSM derived self-consistently from the mass-loss history of the progenitor system; in this way, the comparison between models derived from different progenitors and observations of Cas A would be able to provide some hints on the nature and mass-loss history of the stripped progenitor of Cas A and, possibly, to shed light on the question whether it was a single star or a member in a binary.

The paper is organized as follows. In Sect. 2 we describe the model setup; in Sect. 3 we discuss the results for the interaction of the SNR with the asymmetric dense shell of CSM; and in Sect. 4 we summarize the main results and draw our conclusions. In Appendix A, we discuss an alternative model for the asymmetric circumstellar shell.

## 2. Problem description and numerical setup

We adopted the numerical setup presented in Paper I and which describes the full development of the remnant of a neutrino-driven SN, following its evolution for  $\approx 2000$  years. The setup is the result of the coupling between a model describing a SN explosion with remarkable resemblance to basic properties of Cas A (model W15-2-cw-IIb; Wongwathanarat et al. 2017) and hydrodynamic (HD) and magneto-hydrodynamic (MHD) simulations that describe the formation of the full-fledged SNR (e.g., Orlando et al. 2016). The 3D SN simulation follows the evolution from about 15 milliseconds after core bounce to the breakout of the shock wave at the stellar surface at about 1 day after the core-collapse. Then, the output of this simulation was used as initial condition for 3D simulations which follow the transition from the early SN phase to the emerging SNR and the subsequent expansion of the remnant through the wind of the progenitor star. A thorough description of the setup can be found in Paper I, while a summary of its main features is provided in Sect. 2.1. In this paper, the setup was used to investigate if some of the features observed in the reverse shock of Cas A can be interpreted as signatures of the interaction of the remnant with an asymmetric shell of dense CSM material, most likely erupted by the progenitor star before its collapse (see Sect. 2.2).

### 2.1. Modeling the evolution from the SN to the SNR

The SN model is described in Wongwathanarat et al. (2017) and considers the collapse of an original  $15 M_{\odot}$  progenitor star (denoted as s15s7b2 in Woosley & Weaver 1995 and W15 in Wongwathanarat et al. 2015) from which its H envelope has been removed artificially (before the collapse) down to a rest of  $\approx 0.3 M_{\odot}$  (the modified stellar model is termed W15-IIb in Wongwathanarat et al. 2017). This is motivated by the evidence that observations of light echoes suggest that Cas A is the remnant of a Type IIb SN (Krause et al. 2008; Rest et al. 2011), so that its progenitor star has shed almost all of its H envelope before to go SN (see also Kamper & van den Bergh 1976; Chevalier & Kirshner 1978). The model also considers a neutrino-energy deposition able to power an explosion with an energy of  $1.5 \times 10^{51}$  erg = 1.5 bethe = 1.5 B (see Wongwathanarat et al. 2013, 2015). After the explosion an amount of  $3.3 M_{\odot}$  of stellar debris was ejected into the CSM. The main model parameters are summarized in Table 1.

The SN model takes into account: the effects of gravity (both self-gravity of the SN ejecta and the gravitational field of a central point mass representing the neutron star that has formed after core bounce at the center of the explosion); the fallback of material on the neutron star; the Helmholtz equation of state (Timmes & Swesty 2000), which includes contributions from blackbody radiation, ideal Boltzmann gases of a defined set of fully ionized nuclei, and arbitrarily degenerate or relativistic electrons and positrons. In addition, the model considers a small  $\alpha$ -network to trace the products of explosive nucleosynthesis that took place during the first seconds of the explosion (see Wongwathanarat et al. 2013, 2015). This nuclear reaction network includes 11 species: protons ( $^1\text{H}$ ),  $^4\text{He}$ ,  $^{12}\text{C}$ ,  $^{16}\text{O}$ ,  $^{20}\text{Ne}$ ,

$^{24}\text{Mg}$ ,  $^{28}\text{Si}$ ,  $^{40}\text{Ca}$ ,  $^{44}\text{Ti}$ ,  $^{56}\text{Ni}$ , and an additional “tracer nucleus”  $^{56}\text{X}$ , which represents Fe-group species synthesized in neutron-rich environments as those found in neutrino-heated ejecta (see Wongwathanarat et al. 2017 for details).

After the shock breakout, the SN model shows large-scale asymmetries in the ejecta distribution. The most striking features are three pronounced Ni-rich fingers that may correspond to the extended shock-heated Fe-rich regions observed in Cas A. These features naturally developed from stochastic processes (e.g. convective overturn and SASI) during the first second after core bounce (Wongwathanarat et al. 2017). These characteristics make the adopted SN model most promising to describe a remnant with properties similar to those observed in Cas A (see also Paper I).

The output of model W15-2-cw-IIb at  $\approx 20$  hours after the core-collapse was used as initial conditions for the 3D HD and MHD simulations which describe the long-term evolution ( $\approx 2000$  years) of the blast wave and ejecta, from the shock breakout to the expansion of the remnant through the CSM. In Paper I, we analyzed three long-term simulations to evaluate the effects of energy deposition from radioactive decay and the effects of an ambient magnetic field by switching these effects either on or off. Here, we reconsidered the models presented in Paper I and modified the geometry and density distribution of the CSM to describe the interaction of the remnant with a dense shell in the CSM.

Our simulations include: i) the effects of energy deposition from the dominant radioactive decay chain  $^{56}\text{Ni} \rightarrow ^{56}\text{Co} \rightarrow ^{56}\text{Fe}$ , by adding a source term for the internal energy which takes into account the energy deposit which can be converted into heat (excluding neutrinos, which are assumed to escape freely) and assuming local energy deposition without radiative transfer<sup>1</sup> (Jeffery 1999; Ferrand et al. 2019); ii) the deviations from equilibrium of ionization, calculated through the maximum ionization age in each cell of the spatial domain (see Orlando et al. 2015); iii) the deviations from electron-proton temperature equilibration, calculated by assuming an almost instantaneous heating of electrons at shock fronts up to  $kT = 0.3$  keV (Ghavamian et al. 2007) and by implementing the effects of Coulomb collisions for the calculation of ion and electron temperatures in the post-shock plasma (Orlando et al. 2015); and iv) the effects of back-reaction of accelerated cosmic rays at shock fronts, following an approach similar to that described in Orlando et al. (2012) by including an effective adiabatic index<sup>2</sup>  $\gamma_{\text{eff}}$  which depends on the injection rate of particles  $\eta$  (i.e., the fraction of CSM particles with momentum above a threshold value,  $p_{\text{inj}}$ , that are involved in the acceleration process; Blasi et al. 2005) but neglecting nonlinear magnetic-field amplification.

The SNR simulations were performed using the PLUTO code (Mignone et al. 2007, 2012) configured to compute intercell fluxes with a two-shock Riemann solver (the linearized Roe Riemann solver in the case of HD simulations and the HLLD ap-

<sup>1</sup> We note that our simplified treatment of energy deposition by radioactive decay assumes that all of the decay energy is deposited in the ejecta without any  $\gamma$ -ray leakage from the inner part of the remnant. Thus, our models are expected to overestimate the effects of decay heating and, possibly, to overlook some features. Nevertheless, as shown in Sect. 3.2, although the effects of decay heating are overestimated in our simulations, the remnant evolution during its interaction with the shell is similar in models either with or without these effects.

<sup>2</sup> This simplified approach takes into account the macroscopic effect caused by particle acceleration, but does not exhaust all possible effects of the fast particles.

**TABLE 1:** Setup for the simulated models that best match the observations<sup>a</sup>.

	Parameter	Value			
SN model W15-2-cw-IIb <sup>b</sup>	$E_{\text{exp}}$	$1.5 \times 10^{51}$ erg = 1.5 B			
	$M_{\text{ej}}$	$3.3 M_{\odot}$			
	$E_{\text{exp}}/M_{\text{ej}}$	$0.45 \text{ B}/M_{\odot}$			
SNR Model	rad. dec.	<b>B</b>	$\eta$	$n_w$ cm <sup>-3</sup>	shell
W15-2-cw-IIb-HD <sup>c</sup>	no	no	0	0.8	no
W15-IIb-sh-HD	no	no	0	0.8	SH1 <sup>d</sup>
W15-IIb-sh-HD-1eta	no	no	$10^{-4}$	0.7	SH1
W15-IIb-sh-HD-10eta	no	no	$10^{-3}$	0.6	SH1
W15-IIb-sh-HD+dec	yes	no	0	0.8	SH1
W15-IIb-sh-MHD+dec	yes	yes	0	0.8	SH1
W15-IIb-sh-HD-1eta-sw	no	no	$10^{-4}$	0.7	SH2 <sup>e</sup>
W15-IIb-sh-HD-1eta-az	no	no	$10^{-4}$	0.7	SH3 <sup>f</sup>

<sup>a</sup> We ran about fifty 3D high-resolution simulations of the SNR, exploring the space of parameters reported in Table 2; we summarize here only the models that best match the observations. <sup>b</sup> Presented in Wongwathanarat et al. (2017). <sup>c</sup> Presented in Paper I. <sup>d</sup> The shell is characterized by the best-fit parameters reported in Table 2 but with  $n_{\text{sh}} = 10 \text{ cm}^{-3}$  and  $\phi = 0$ . <sup>e</sup> The shell is the same as in SH1 but rotated by  $90^\circ$  clockwise about the  $y$  axis. <sup>f</sup> The shell is the same as in SH1 but with density  $n_{\text{sh}} = 20 \text{ cm}^{-3}$  and  $\phi = 50^\circ$  (see Table 2).

proximate Riemann solver in the case of MHD simulations; see Paper I for more details). The HD/MHD equations were solved in a 3D Cartesian coordinate system  $(x, y, z)$ , assuming the Earth vantage point to lie on the negative  $y$ -axis. The remnant is oriented in such a way that the Fe-rich fingers developed soon after the core bounce point toward the same direction as the extended Fe-rich regions observed in Cas A (see Paper I). The large physical scales spanned from the shock breakout to the full-fledged remnant at the age of 2000 years were followed by gradually extending the computational domain (a Cartesian box covered by a uniform grid of  $1024^3$  zones) as the forward shock propagates outward. The spatial resolution varies between  $\approx 2.3 \times 10^{11}$  cm (on a domain extending between  $-1.2 \times 10^{14}$  cm and  $1.2 \times 10^{14}$  cm in all directions) at the beginning of the calculation to  $\approx 0.018$  pc (on a domain extending between  $-9.4$  pc and  $9.4$  pc) at the end.

First we evaluated the effects of back-reaction of accelerated cosmic rays on the results by considering simulations either with (models W15-IIb-sh-HD-1eta and W15-IIb-sh-HD-10eta) or without (W15-IIb-sh-HD) the modifications of the shock dynamics due to cosmic rays acceleration at both the forward and reverse shocks. We considered two cases:  $\eta = 10^{-4}$  and  $\eta = 10^{-3}$ , leading to  $\gamma_{\text{eff}} \approx 3/2$  (model W15-IIb-sh-HD-1eta) and  $\gamma_{\text{eff}} \approx 4/3$  (model W15-IIb-sh-HD-10eta), respectively (see Fig. 2 in Orlando et al. 2016). The former case is the most likely for Cas A, according to Orlando et al. (2016); the latter is an extreme case of a very efficient particle acceleration. For the sake of simplicity, in the present calculations we did not assume a time dependence of  $\gamma_{\text{eff}}$ , i.e., we assumed that the lowest value is reached immediately at the beginning of the simulation.

In Paper I, we found that the energy deposition from radioactive decay provides an additional pressure to the plasma which inflates ejecta structures rich in decaying elements. Thus, we performed an additional simulation (W15-IIb-sh-HD+dec) analogous to model W15-IIb-sh-HD but including the effects of energy deposition from radioactive decay. We investigated these

effects on the remnant-shell interaction by comparing models W15-IIb-sh-HD and W15-IIb-sh-HD+dec.

We have also investigated the possible effects of an ambient magnetic field on the remnant-shell interaction. In fact, although the magnetic field does not affect the overall evolution of the remnant, it may limit the growth of HD instabilities that develop at the contact discontinuity or during the interaction of the forward shock with inhomogeneities of the CSM (see, for instance, Orlando et al. 2019a) as, in the present case, the circumstellar shell. Hence, following Paper I, we performed a simulation as model W15-IIb-sh-HD+dec but including an ambient magnetic field (model W15-IIb-sh-MHD+dec) and compared the two models. As in Paper I, we adopted the ambient magnetic field configuration described by the ‘‘Parker spiral’’ resulting from the rotation of the progenitor star and from the corresponding expanding stellar wind (Parker 1958); the adopted pre-SN magnetic field has an average strength at the stellar surface  $B_0 \approx 500$  G (Donati & Landstreet 2009).

A few words of caution are needed about the adopted magnetic field. In fact, the pre-SN field strength and configuration are unknown in Cas A and our choice is, therefore, arbitrary. Furthermore, typical magnetic field strengths in post-shock plasma inferred from observations of Cas A are of the order of 0.5 mG (e.g., Sato et al. 2018), whereas the pre-SN magnetic field is of the order of  $0.2 \mu\text{G}$  at a distance of 2.5 pc from the center of explosion and the highest values of magnetic field strength in post-shock plasma at the age of Cas A are of the order of  $10 \mu\text{G}$  in our MHD simulation (model W15-IIb-sh-MHD+dec). These observations suggest that some mechanism of magnetic field amplification is at work, such as turbulent motion in the post-shock plasma (e.g., Giacalone & Jokipii 2007; Inoue et al. 2009 and references therein) and/or non-linear coupling between cosmic rays and background magnetic field (Bell 2004). The former requires quite high spatial resolution and the latter solving the evolution of the non-linear coupling in a short time-scale and length-scale. In fact, both these mechanisms are not included in our MHD simulations that describe the evolution of the whole remnant. In light of this, we expect that stronger fields may have effects on the remnant-shell interaction not included in our models especially for the acceleration of particles (most likely correlated with the magnetic field amplification) and the growth of HD instabilities. Consequently, the synthesis of radio emission presented in Sect. 3.3 is expected to predict radio images which cannot be directly compared with radio observations of Cas A. Nevertheless, these synthetic maps were derived with the aim to identify the position of the reverse shock during the remnant-shell interaction. Since the position and resulting overall shape of the reverse shock do not depend on the particular configuration of the magnetic field adopted, the maps can be safely used for our purposes.

## 2.2. The inhomogeneous CSM

In Paper I, the remnant was described as expanding through the spherically symmetric wind of the progenitor star. The wind density was assumed to be proportional to  $r^{-2}$  (where  $r$  is the radial distance from the center of explosion) and was equal to  $n_w = 0.8 \text{ cm}^{-3}$  (consistent with the values of post-shock wind density inferred from observations of Cas A; Lee et al. 2014) at the radius  $r_{\text{fs}} = 2.5$  pc, namely the nominal current outer radius of the remnant (at a distance of  $\approx 3.4$  kpc). Assuming a wind speed of  $10 - 20 \text{ km s}^{-1}$  (typical values for the wind during the red supergiant phase), the estimated mass-loss rate is  $\dot{M} \approx 2 - 4 \times 10^{-5} M_{\odot} \text{ yr}^{-1}$ . Furthermore, a progressive flatten-

ing of the wind profile to a uniform density  $n_c = 0.1 \text{ cm}^{-3}$  was considered at distances  $> 3 \text{ pc}$  (where we ignore the structure of the still unshocked CSM) to prevent unrealistic low values of the density.

Here, we aim at exploring the effects of a dense shell of CSM on the evolution of the remnant and at testing the hypothesis that some of the features observed in the reverse shock of Cas A may be interpreted as signatures of a past interaction of the remnant with an asymmetric circumstellar shell. Deriving an accurate reconstruction of the pre-SN CSM around Cas A is well beyond the scope of the paper. Thus, for our purposes, we adopted an idealized and parametrized description of the CSM which consists of a spherically symmetric wind (as in Paper I) and a shell of material denser than the wind. We also allowed the shell to be asymmetric with one hemisphere being denser than the other. In fact, several lines of evidence suggest that the CSM around massive stars can be characterized by the presence of asymmetric and dense circumstellar shells, resulting from episodic massive eruptions during the late stages of star evolution (e.g., Smith et al. 2014; Levesque et al. 2014; Graham et al. 2014).

The asymmetry was modeled with an exponential density stratification along a direction with unit vector  $\mathbf{D}$ , which defines the symmetry axis of the shell. This dipole asymmetry with the enhancement covering  $2\pi$  steradians is made simply to differentiate the two hemispheres of the shell; one might expect an enhancement occupying a smaller solid angle (as seen from the explosion center) to produce similar effects on the reverse shock dynamics over a smaller range of azimuth. The transition from the shell to the wind was modulated by a Gaussian function. The exponential and Gaussian functions were selected to allow for a smooth transition between the wind and the shell. Considering the orientation of the remnant in the 3D Cartesian coordinate system (see Sect. 2.1), the density distribution of the CSM is given by:

$$n = n_w \left( \frac{r_{\text{fs}}}{r} \right)^2 + n_{\text{sh}} \exp \left[ -\frac{(r - r_{\text{sh}})^2}{2\sigma^2} \right] \exp \left[ \frac{\mathbf{r} \cdot \mathbf{D}}{H} \right], \quad (1)$$

where  $n_w$  has a value between  $0.6 \text{ cm}^{-3}$  and  $0.8 \text{ cm}^{-3}$ , depending on the injection efficiency (see Orlando et al. 2016),  $r_{\text{fs}} = 2.5 \text{ pc}$ ,  $n_{\text{sh}}$  is a reference density of the shell,  $r_{\text{sh}}$  is the shell radius,  $\sigma$  represents the shell thickness,  $H$  is the scale length of the shell density,  $\mathbf{r} \cdot \mathbf{D} = x \cos \theta \cos \phi - y \sin \phi + z \sin \theta \cos \phi$ , and  $\theta$  and  $\phi$  are the angles measured: the former in the  $[x, z]$  plane (i.e., around the  $y$ -axis) counterclockwise from the  $x$ -axis (i.e., from the west) and the latter about the  $z$ -axis counterclockwise from the  $[x, z]$  plane<sup>3</sup> (i.e., from the plane of the sky). We note that the parameter  $H$  determines the contrast between the densest and least dense portions of the shell and, therefore, the level of asymmetry introduced between the two remnant hemispheres.

As a first step, we explored the space of parameters of the shell, assuming that  $\mathbf{D}$  (i.e., the symmetry axis of the shell) lies in the plane of the sky ( $[x, z]$  plane) and, therefore, is perpendicular to the line-of-sight (LoS). In this case,  $\phi = 0$  and  $\mathbf{r} \cdot \mathbf{D} = x \cos \theta + z \sin \theta$ . An example of pre-SN CSM resulting in this last case, for  $\theta = 30^\circ$ , is shown in Fig. 2. Considering that the Earth vantage point lies on the negative  $y$ -axis, the shell has the maximum density in the north-west (NW) quadrant and the minimum density in the south-east (SE) quadrant.

As a second step, we explored the possibility that  $\mathbf{D}$  forms an angle  $\phi > 0$  with the plane of the sky in Eq. 1. In other words,

<sup>3</sup> So that the unit vector  $\mathbf{D}$  has components:  $D_x = \cos \theta \cos \phi$ ,  $D_y = -\sin \phi$  and  $D_z = \sin \theta \cos \phi$ .

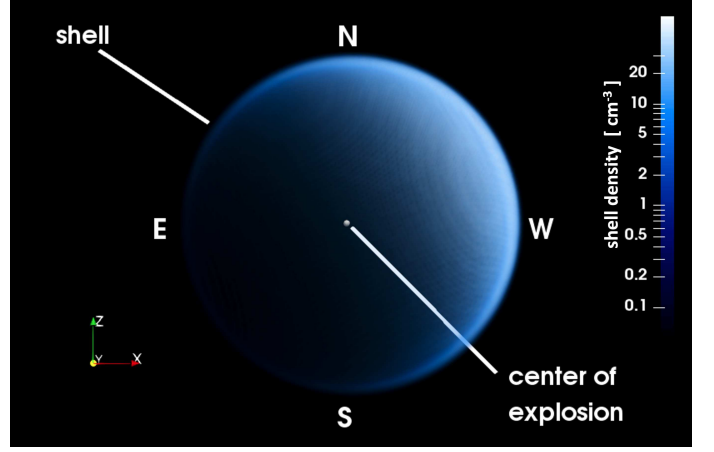


Fig. 2: Schematic representation of the massive circumstellar shell. The center of the explosion is coincident with the geometric center of the spherical shell. The Earth vantage point lies on the negative  $y$ -axis. In this representation the angles in Eq. 1 are  $\theta = 30^\circ$  and  $\phi = 0$  and the shell has the maximum density in the NW quadrant and the minimum density in the SE quadrant.

we explored models in which the shell was also denser in its blueshifted nearside than in the redshifted farside, as suggested by the evidence that the large majority of QSFs is at blue shifted velocities (Reed et al. 1995). In Sect. 3.4, we discuss the results of this exploration and present model W15-IIb-sh-HD-1eta-az, our favorite model (with  $\phi = 50^\circ$ ) to describe the dynamics of the reverse and forward shocks observed in Cas A.

### 3. Results

We ran 3D high-resolution simulations of the SNR, searching for the parameters of the shell (density, radius, and thickness) and of its degree of asymmetry (the angles  $\theta$  and  $\phi$  and the density scale length) which can reproduce the slow down of the reverse shock velocity in the western region of Cas A, the offset between the geometric centers of the reverse and forward shocks as inferred from the observations, and the evidence that the non-thermal emission from the reverse shock in the western region is brighter than in the eastern region, simultaneously. Table 2 reports the shell parameters of our simulations most closely reproducing the observations and the range of values explored. The Table also reports the total mass calculated for the shell. We note that this mass depends on the geometry of the shell adopted. We expect that a smaller or partial shell or a shell with a shape deviating from spherical symmetry (for instance, more elongated on one side) may produce similar observables with a different mass.

In Sect. 3.1, we discuss in detail the interaction of the remnant with the dense shell for one of our simulations with  $\phi = 0$  in Eq. 1 more closely resembling the observations (model W15-IIb-sh-HD-1eta). Then, in Sect. 3.2 we describe how the remnant evolution changes using different shell parameters. Finally, in Sects. 3.3 and 3.4 we analyze the remnant asymmetries caused by the interaction of the remnant with the shell, including also the case with  $\phi > 0$  (in Sect. 3.4), and compare the model results with observations.

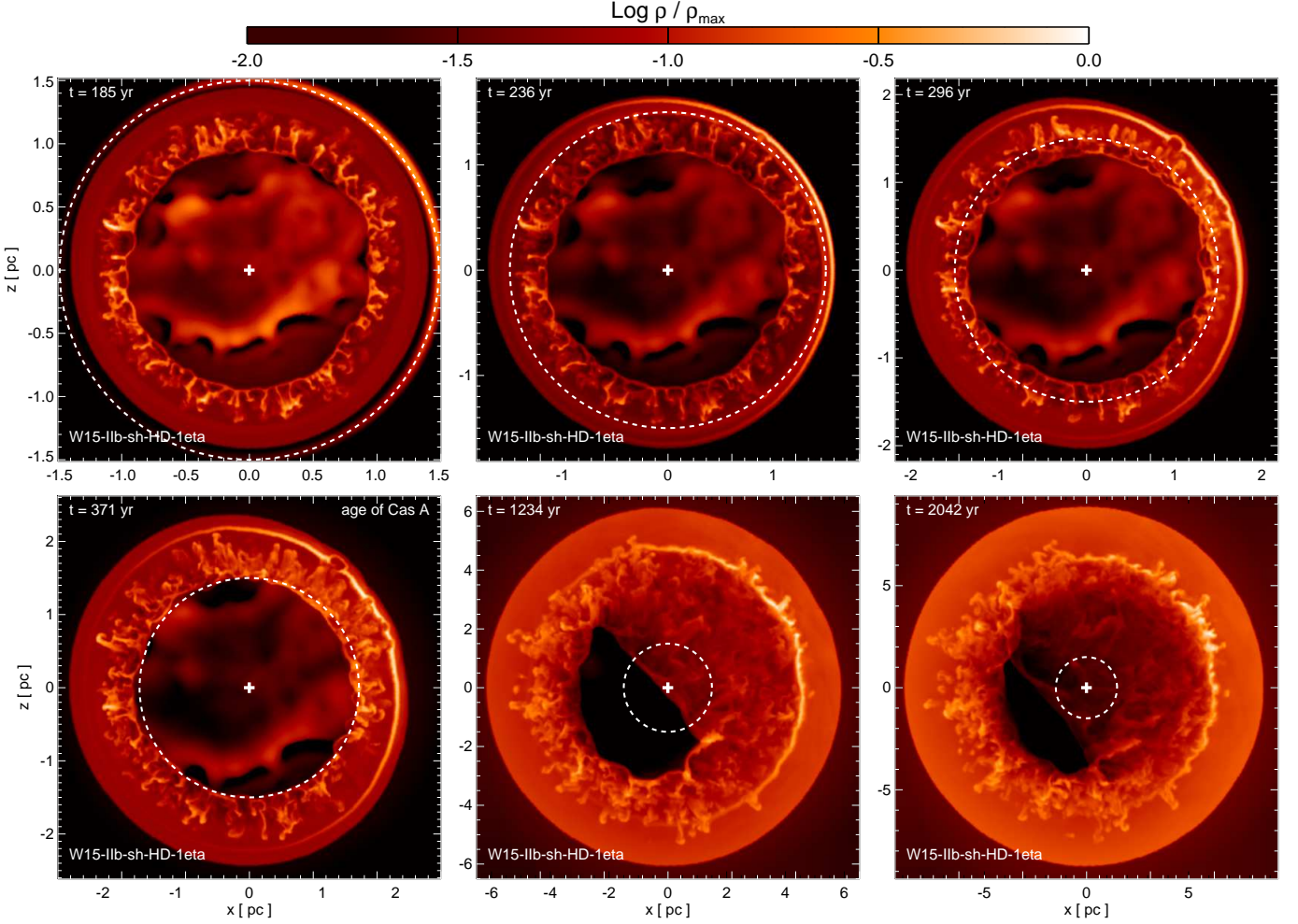


**FIG. 3:** 2D sections in the  $(x, z)$  plane of the spatial density distribution of shocked plasma (in log scale) at the labeled times for model W15-IIb-sh-HD-1eta. Each image has been normalized to its maximum,  $\rho_{\max}$ , for visibility. The dashed circle in each panel marks the pre-shock position of the dense shell in the  $(x, z)$  plane; the cross shows the center of the explosion.

### 3.1. Interaction of the remnant with the dense shell

The evolution of the remnant in the phase before the interaction of the blast wave with the shell is analogous to that presented in Paper I. Initially the metal-rich ejecta expand almost homologously, though in models including the radioactive decay significant deviations are present in the innermost ejecta (rich in  $^{56}\text{Ni}$  and  $^{56}\text{Co}$ ) due to heating caused by the decay chain  $^{56}\text{Ni} \rightarrow ^{56}\text{Co} \rightarrow ^{56}\text{Fe}$ . These effects decrease fast with time and are significant only during the first year of evolution. Thus, after this initial inflation of Fe-rich ejecta, we expect that the qualitative evolution of the remnant is similar in models either with or without the radioactive decay effects included (see Paper I). In all the models, the Fe-group elements start to interact with the reverse shock about  $\approx 30$  years after the SN when almost all  $^{56}\text{Ni}$  and  $^{56}\text{Co}$  have already decayed to stable  $^{56}\text{Fe}$  (see Paper I for details).

In our simulations best matching the observations (all reported in Table 1), the dense shell of CSM has a radius  $r_{\text{sh}} = 1.5$  pc. In model W15-IIb-sh-HD-1eta, the blast wave starts to interact with the shell  $\approx 180$  years after the SN event (see upper left panel in Fig. 3). The NW side of the shell is hit first due to the large-scale asymmetries of the blast wave inherited from the

earliest moments of the explosion<sup>4</sup> (see Paper I). At the beginning of the interaction, the forward shock slows down because of the propagation through a medium denser than the  $r^{-2}$  wind density distribution. Consequently, the distance between the forward and reverse shock gradually decreases. This effect is the largest in the NW side which is hit earliest and where the CSM shell in our reference model has the highest density. This is also evident in Fig. 4 showing the forward and reverse shock radii in the NW and SE hemispheres of the remnant: the forward shock in the NW side shows a slow down in its expansion at the time of interaction with the shell that is not present in the SE side. This further enhances the degree of asymmetry in the remnant, leading to a thickness of the mixing region between the forward and reverse shocks that is the smallest in the NW side. The shell is fully shocked at  $t \approx 240$  years (upper center panel in Fig. 3). At later times, the forward shock travels again through the  $r^{-2}$  wind density distribution and its velocity gradually increases to the values expected without the interaction with the shell.

<sup>4</sup> Note that the large-scale asymmetry of the SN explosion points to the NW in the redshifted side of the remnant (see Paper I), while the densest part of the shell lies in the NW quadrant of the plane of the sky. Their projections into the plane of the sky coincide by chance.

**TABLE 2:** Explored and favorite parameters of the shell in the CSM for the models of Cas A<sup>a</sup>. The favorite parameters correspond to those of model W15-IIb-sh-HD-1eta-az in Table 1.

Parameter	Units	Range Explored	Favorite Value
$n_{\text{sh}}$	( $\text{cm}^{-3}$ )	[5; 20]	20 <sup>b</sup>
$r_{\text{sh}}$	(pc)	[1; 2]	1.5
$\sigma$	(pc)	[0.02; 0.05]	0.02
$\theta$		[35°; -57°]	30°
$\phi$		[0°; 50°]	50°
$H$	(pc)	[0.35; 3.5]	0.7
$M_{\text{sh}}$	( $M_{\odot}$ )	[0.43; 3.71]	2.3 <sup>c</sup>
$M_{\text{SE}}$	( $M_{\odot}$ )	[0.16; 0.49]	0.7
$M_{\text{NW}}$	( $M_{\odot}$ )	[0.22; 3.22]	1.6
$n_{\text{SE}}$	( $\text{cm}^{-3}$ )	[1.6; 5.8]	6.3
$n_{\text{NW}}$	( $\text{cm}^{-3}$ )	[6.7; 89]	77

<sup>a</sup> The reference density of the shell,  $n_{\text{sh}}$ , the shell radius and thickness,  $r_{\text{sh}}$  and  $\sigma$ , the angle  $\theta$  (measured in the plane of the sky, about the  $y$ -axis, counterclockwise from the west), the angle  $\phi$  (measured about the  $z$ -axis counterclockwise from the plane of the sky) and the scale length of the shell density,  $H$ , are used in Eq. 1 to describe the CSM. The total mass of the shell,  $M_{\text{sh}}$ , the masses of the SE and NW hemispheres of the shell,  $M_{\text{SE}}$  and  $M_{\text{NW}}$ , and the peak densities of the shell in the SE and NW directions,  $n_{\text{SE}}$  and  $n_{\text{NW}}$ , are derived from the simulations. <sup>b</sup> The density  $n_{\text{sh}} = 10 \text{ cm}^{-3}$  if  $\phi = 0$ . <sup>c</sup> The mass of the shell is  $M_{\text{sh}} = 1.3 M_{\odot}$  if  $\phi = 0$ .

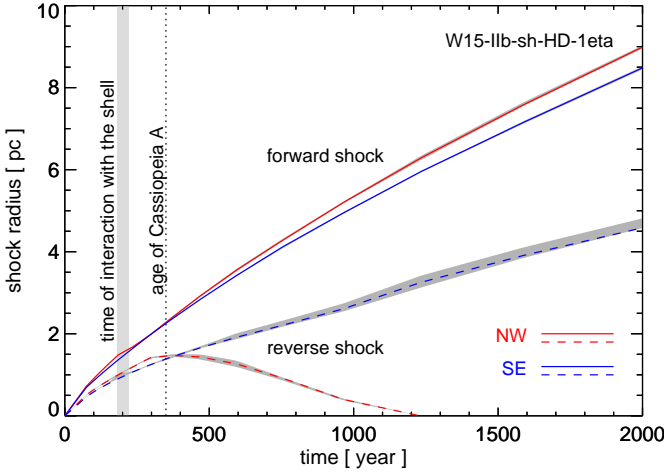


**FIG. 4:** Radii of the forward (solid lines) and reverse (dashed lines) shocks versus time in the NW (red lines) and SE (blue lines) hemispheres for model W15-IIb-sh-HD-1eta. The shock positions are averaged over solid angles (as seen from the explosion center) of  $10^\circ$  around the NW and SE directions. The vertical dotted line marks the approximate age of Cas A; the shaded rectangular box marks the time of remnant-shell interaction. The grey bands under the colored average curves indicate the range of shock positions at each time in the solid angles examined.

The remnant-shell interaction drives a reflected shock that travels inward through the mixing region and that is the most energetic where the shell is the densest. The inward propagating shock wave reaches the reverse shock at  $t \approx 290$  years (upper right panel in Fig. 3). As a result, the reverse shock velocity in the observer frame decreases and, again, the effect is the largest (with velocities equal to zero or even negative) in the NW side where the reflected shock is the most energetic (Fig. 4). At the

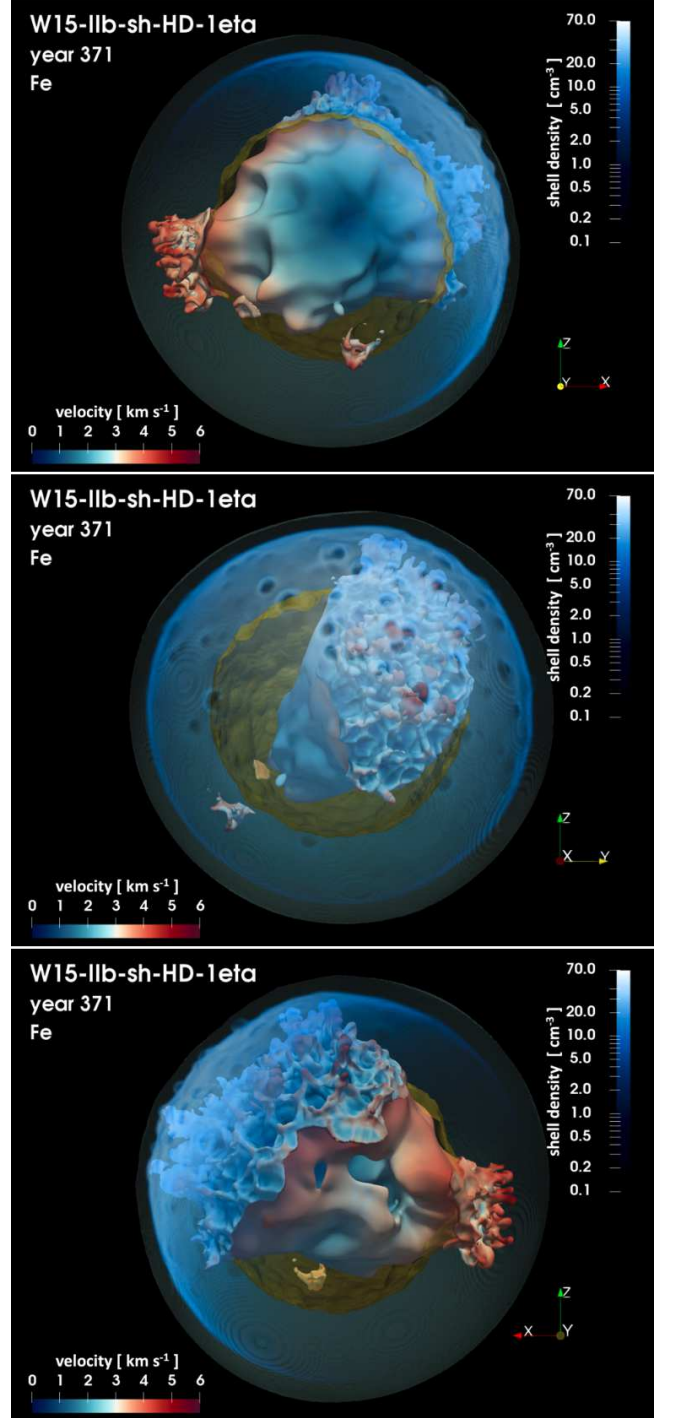


**FIG. 5:** Isosurface of the distribution of Fe (corresponding to a value of Fe density which is at 5% of the peak density) at the age of Cas A for different viewing angles for model W15-IIb-sh-HD-1eta; the colors give the radial velocity in units of  $1000 \text{ km s}^{-1}$  on the isosurface (color coding defined at the bottom of each panel). The semi-transparent clipped quasi-spherical surfaces indicate the forward (green) and reverse (yellow) shocks. The shocked shell is visualized through a volume rendering that uses the blue color palette (color coding on the right of each panel); the opacity is proportional to the plasma density. A navigable 3D graphic of this model is available at <https://skfb.ly/o8FnO>.

age of Cas A, the reverse shock in the NW hemisphere has already started to move inward in the observer frame (see Fig. 4) and the remnant shows the effects of the interaction with the shell

(lower left panel in Fig. 3). As a result, the mixing region is less extended and the density of the shocked plasma is higher in the western than in the eastern region.

Fig. 5 shows the spatial distribution of Fe at the age of Cas A in model W15-IIb-sh-HD-1eta. The effects of back-reaction of accelerated cosmic rays do not change significantly this distribution (models W15-IIb-sh-HD and W15-IIb-sh-HD-10eta show similar results), whilst the decay of radioactive species leads to the inflation of the Fe-rich plumes in models W15-IIb-sh-HD+dec and W15-IIb-sh-MHD+dec (see Paper I). The figure shows different viewing angles, namely with the perspective on the negative  $y$ -axis (i.e., the vantage point is at Earth; upper panel), on the positive  $x$ -axis (middle panel), and on the positive  $y$ -axis (i.e., the vantage point is from behind Cas A; lower panel). At this time about 35% of Fe has already passed through the reverse shock (see Fig. 5 in Paper I), leading to the formation of large regions of shocked Fe-rich ejecta in coincidence with the original large-scale fingers of Fe-group elements (see Paper I for more details). The shocked dense shell of CSM has already started to interact with the fingers of ejecta developed by HD instabilities (Rayleigh-Taylor, Richtmyer-Meshkov, and Kelvin-Helmholtz shear instability; Gull 1973; Fryxell et al. 1991; Chevalier et al. 1992). In particular, the figure shows Fe-rich shocked filamentary structures, which extend from the contact discontinuity toward the forward shock. These fingers protrude into the shocked shell material, producing holes in the shell (see middle panel in Fig. 5) and driving the mixing between stellar and shell material. The fingers in the NW side are closer to the forward shock than in the SE side, due to the reduced distance between the contact discontinuity and the forward shock where the shell is the densest. The radial velocity of the fingers in the NW side is smaller than in the SE (see the color code of the isosurface in Fig. 5) due to the passage of the inward shock, which is the most energetic in the NW. This is consistent with observations (e.g., Willingale et al. 2002).

At later times, the degree of asymmetry of the reverse shock structure largely increases due to the fastest inward propagation of the reverse shock in the NW region (see Fig. 4). At the age of  $\approx 1000$  yr, the reverse shock is highly asymmetric and reaches the center of the explosion from NW (see lower center panel in Fig. 3 and Fig. 4). Then, it starts to propagate through the ejecta traveling outward in the SE portion of the remnant (lower right panel in Fig. 3). In the meantime, the forward shock continues to travel through the  $r^{-2}$  wind density distribution with roughly the same velocity in all directions. The forward shock appears to be spherically symmetric at the end of the simulation, when the remnant has a radius  $R \approx 9$  pc and an age of  $\approx 2000$  yr. It is interesting to note that, at this age, the signatures of the remnant-shell interaction are clearly visible in the reverse shock, whilst the forward shock apparently does not keep memory of the past interaction (see Fig. 4).

### 3.2. Effects of shell parameters on the remnant evolution

We explored the space of parameters of the shell by performing about fifty simulations. The parameters explored are (see Table 2): the reference density of the shell,  $n_{\text{sh}}$ , the shell radius and thickness,  $r_{\text{sh}}$  and  $\sigma$ , the angle  $\theta$  (measured counterclockwise from the west; see Eq. 1), and the scale length of the shell density,  $H$ . For this exploration, the angle  $\phi$  was fixed equal to zero; its effect is investigated in Sect. 3.4. The parameter space was explored adopting an iterative process of trial and error to converge on model parameters that qualitatively reproduce the profiles of the forward and reverse shock velocities versus the

position angle in the plane of the sky at the age of Cas A (e.g., Vink et al. 2022; see also Fig. 6 and Sect. 3.3). We note that our models do not pretend to be able to reconstruct the structure of the pre-SN circumstellar shell but they aim to test the possibility that the inward-moving reverse shock observed in the western hemisphere of Cas A can be interpreted as the signature of a past interaction with a circumstellar shell. From our exploration, we found that the models producing velocity profiles, which more closely reproduce the observations (listed in Table 1), are characterized by the common set of parameters listed in Table 2 with  $n_{\text{sh}} = 10 \text{ cm}^{-3}$  if  $\phi = 0$  (see the favorite values).

The exploration of the parameter space was limited to asymmetric shells with the densest side in the western hemisphere of the remnant, namely where the profile of the reverse shock velocity has a minimum (see Fig. 6). The shell asymmetry is regulated by the angle  $\theta$  and the scale length of the shell density,  $H$ . The former parameter determines where the shell is the densest in the plane of the sky, so that the effects of interaction with the shell are the largest and the reverse shock velocity has a minimum. Larger (lower) values of  $\theta$  determine a shift of the minimum shock velocity toward the north (south) in Fig. 6. The parameter  $H$  regulates the density contrast between the two hemispheres of the shell (namely its densest and least dense portions) and, therefore, the level of asymmetry introduced by the shell: the higher the value of  $H$  the smaller the contrast between the reverse shock velocities in the two remnant hemispheres.

In simulations assuming a shell radius smaller than  $r_{\text{sh}} = 1.5$  pc, the remnant starts to interact with the shell at an earlier time. Hence, the reverse shock starts earlier to move inward where the shell is dense, leading to a reverse shock structure that significantly deviates from the spherical shape at the age of Cas A (this happens at later times in our favorite simulations listed in Table 1): a result which is at odds with observations. On the other hand, in simulations with a higher shell radius, the forward shock in the western hemisphere still has expansion velocities much lower than those in the eastern hemisphere (producing an evident minimum in the profiles in Fig. 6) because it did not have the time to re-accelerate to the velocity values expected when it propagates through the wind of the progenitor star.

The shell density regulates the slow down of the forward shock traveling through the shell and the strength of the inward shock. In models with a shell denser than in our favorite cases (listed in Table 1), the slow down of the forward shock is higher, leading to a minimum in its velocity profile at the age of Cas A (at odds with observations; see Fig. 6), and the inward shock is stronger, leading to a deeper minimum in the profile of the reverse shock (inward velocities lower than the minimum values observed, namely  $\approx -2000 \text{ km s}^{-1}$ ). On the other hand, models with a shell less dense than in our favorite models produce a minimum in the velocity profile of the reverse shock with velocities higher than observed ( $> -2000 \text{ km s}^{-1}$ ). A similar role is played by the thickness of the shell,  $\sigma$ : a thicker (thinner) shell produces larger (smaller) effects on the forward and reverse shock dynamics. In principle, one could trade off density and thickness to produce similar results. However, we found that, in simulations with higher values of  $\sigma$ , the reverse shock deviates from the spherical shape at the age of Cas A if the interaction of the remnant with the thicker shell starts at earlier times than in our favorite models; conversely, if the interaction starts at the time of our favorite simulations, the forward shock shows a minimum in its velocity profile because it left the thicker shell too late and it did not have time to re-accelerate.

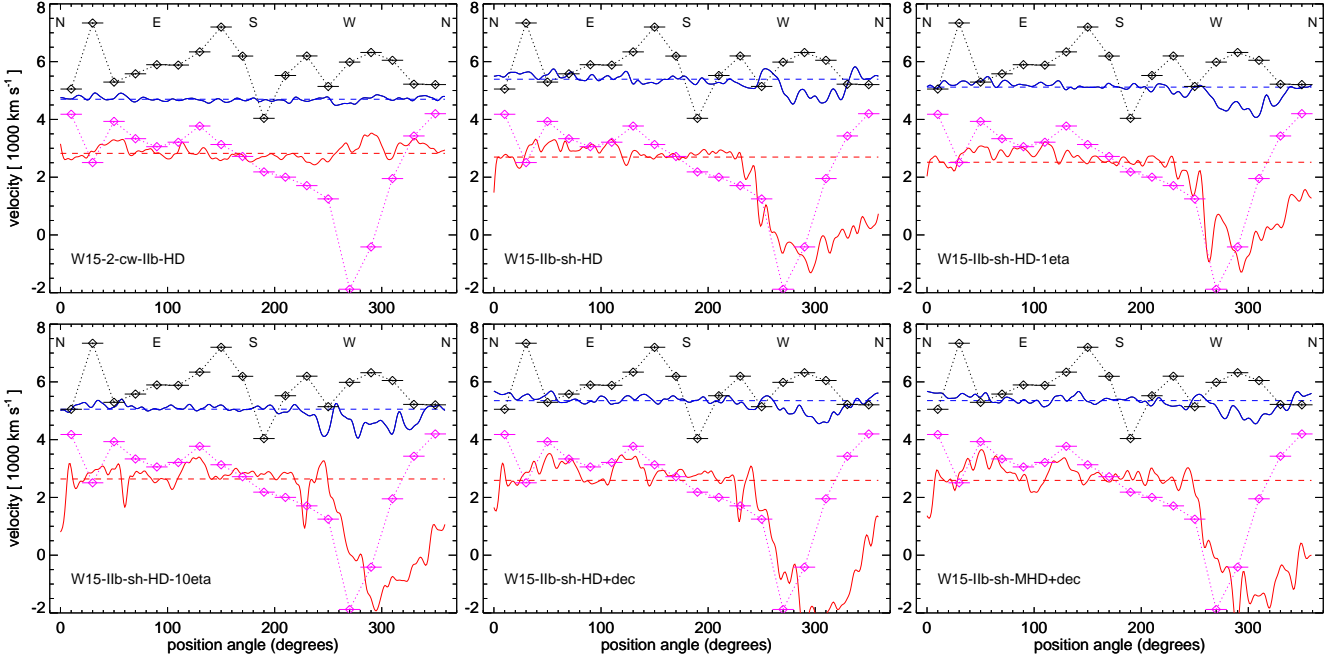


**FIG. 6:** Forward (blue) and reverse (red) shock velocities versus the position angle in the plane of the sky at the age of Cas A for the first six SNR models listed in Table 1, including model W15-2-cw-IIb-HD presented in Paper I. The dashed horizontal lines mark the median values of the respective velocities. The velocities of the forward (black diamonds) and reverse (magenta diamonds) shocks derived from the analysis of Chandra observations (Vink et al. 2022) are overplotted for comparison.

Including the effects of radioactive decay does not qualitatively change the evolution of the remnant and its interaction with the shell. As shown in Paper I, the energy deposition by radioactive decay provides additional pressure to the plasma, which inflates structures with a high mass fraction of decaying elements against the surroundings. Thus, the expansion of the ejecta is powered by this additional pressure and the remnant expands slightly faster than in the case without these effects taken into account. As a consequence, the remnant starts to interact with the shell slightly earlier in models W15-IIb-sh-HD+dec and W15-IIb-sh-MHD+dec than in the others. The reflected shock from the shell reaches the reverse shock at earlier times. Thus, at the age of Cas A, the reverse shock in the NW region moves inward in the observer frame with slightly higher velocities than in models without radioactive decay (e.g., compare models W15-IIb-sh-HD and W15-IIb-sh-HD+dec in Fig. 6). The differences between the models, however, are moderate ( $< 30\%$ ).

As for the effect of an ambient magnetic field, it does not, as expected, influence the overall dynamics of the forward and reverse shocks. Model W15-IIb-sh-MHD+dec (the only one including the magnetic field) shows an evolution similar to that of model W15-IIb-sh-HD+dec. The main effect of the magnetic field is to limit the growth of HD instabilities at the contact discontinuity due to the tension of the magnetic field lines which maintain a more laminar flow around the fingers of dense ejecta gas that protrude into the shocked wind material (e.g., Orlando et al. 2012). Indeed the post-shock magnetic field is heavily modified by the fingers and the field lines wrap around these ejecta structures, leading to a local increase of the field strength. The interaction of the remnant with the shell leads to a further compression of the magnetic field, which is more effective in the NW region where the shell is the densest. There the post-shock magnetic field reaches values of the order of  $10 \mu\text{G}$

when the pre-SN field strength at 2.5 pc was  $0.2 \mu\text{G}$ . As a result, the field strength is significantly higher in the NW than in the SE region of the remnant and this contributes in determining an asymmetry in the brightness distribution of the nonthermal emission in the two hemispheres. Note that model W15-IIb-sh-MHD+dec neglects the magnetic field amplification due to back-reaction of accelerated cosmic rays, so that the enhancement of magnetic field in the NW is purely due to the high compression of field lines during the interaction of the remnant with the shell. Field strengths higher by an order of magnitude (and consistent with observations) may be reached due to magnetic field amplification.

### 3.3. Reverse shock asymmetries at the age of Cas A

The interaction of the remnant with the asymmetric shell affects the propagation of the reverse shock in a different way in the eastern and western sides. This is evident from an inspection of Fig. 6, which shows the profiles of the forward and reverse shock velocities versus the position angle in the plane of the sky at the age of Cas A. For comparison, the figure also shows the profiles derived from a model not including the interaction of the remnant with the shell (upper left panel; model W15-2-cw-IIb-HD presented in Paper I) and the profiles derived from the analysis of Chandra observations of Cas A (black and magenta diamonds; Vink et al. 2022). At the age of Cas A, the models describing the interaction with the shell show a forward shock that propagates with velocity between  $5000 \text{ km s}^{-1}$  and  $6000 \text{ km s}^{-1}$  at all position angles, thus producing results analogous to those derived from the model without the shell and in agreement with observations. This is a sign that the effect of the interaction of the forward shock with the shell has run out and, in fact, in all

the models the forward shock propagates through the  $r^{-2}$  wind density distribution<sup>5</sup>.

Conversely, the velocity of the reverse shock shows strong changes with the position angle if the remnant interacts with the shell, at odds with model W15-2-cw-I Ib-HD that shows a reverse shock velocity around  $\approx 3000 \text{ km s}^{-1}$  at all position angles. In the eastern side, where the shell is tenuous, the evolution of the reverse shock is only marginally affected by the shell and the shock propagates with a velocity of  $\approx 3000 \text{ km s}^{-1}$  (as in model W15-2-cw-I Ib-HD); in the western side, where the shell is dense, the reverse shock is slowed down by the reflected shock driven by the interaction with the shell and, as a result, the reverse shock appears to move inward in the observer frame as observed in Cas A. Fig. 6 shows that the agreement between models and observations is remarkable, producing a reverse-shock minimum roughly where it is observed. However, we also note that the predicted minimum is broader than observed, extending further to the north. This suggests that the high density portion of the modeled shell is too large (the match with the data would improve if the high density portion of the shell subtends a smaller solid angle as seen from the explosion center) or that the actual shell is incomplete or irregular (and not with a regular spherical shape as assumed).

We note that Sato et al. (2018) report bright nonthermal X-ray emitting features in the interior of Cas A due to inward-moving shocks in the western and southern hemispheres (see also Anderson & Rudnick 1995; Keohane et al. 1996; DeLaney et al. 2004; Helder & Vink 2008). These features are not reproduced by our models which predict an inward-moving reverse shock only in the NW hemisphere. Features similar to those observed by Sato et al. (2018) might be obtained by rotating the asymmetric shell approximately  $90^\circ$  clockwise about the  $y$  axis. In this case, however, we found that the models do not reproduce other asymmetries that characterize the reverse shock of Cas A, in particular the velocity profiles derived by Vink et al. (2022) and the orientation of the offset between the geometric center of the reverse shock and that of forward shock (Gotthelf et al. 2001). In Appendix A, we present an example of these models. Here we preferred to discuss the models that most closely reproduce many (but not all) of the reverse shock asymmetries observed in Cas A. Nevertheless, our study clearly shows that the interaction of the remnant with local asymmetric density enhancements (as the densest portion of the shell in our simulations) can produce inward-moving reverse shocks there. In case of a shell with a more complex structure (e.g., more fragmented) than modeled here, it may be possible to reproduce the locations where inward-moving shocks are observed if density enhancements are placed in the same locations.

The negative velocity of the reverse shock in the NW side has important consequences on the acceleration of particles. In fact, the ejecta enter the reverse shock with a higher relative velocity in the western than in eastern side. Fig. 7 shows the velocities of ejecta when they enter the reverse shock at the different position angles. The velocity is below  $2000 \text{ km s}^{-1}$  for most of the position angles, except in the western part, where the ejecta enter the reverse shock with a velocity between  $4000$  and  $7000 \text{ km s}^{-1}$ . This implies that, only in the western part, the reverse shock is potentially able to accelerate electrons to high enough energies to emit X-ray synchrotron radiation: its velocity relative to the

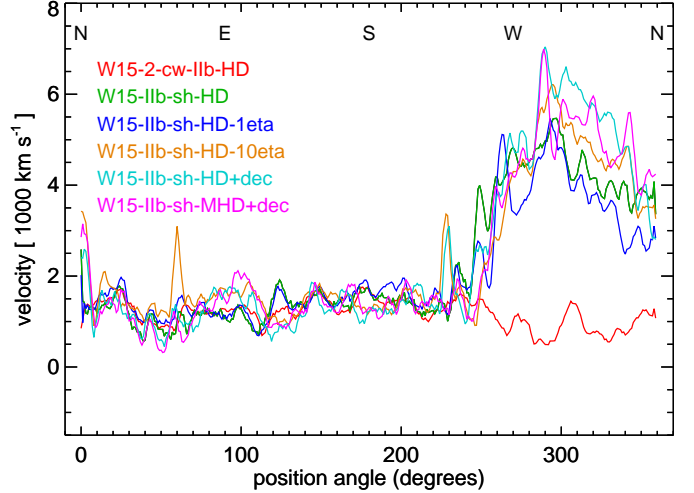
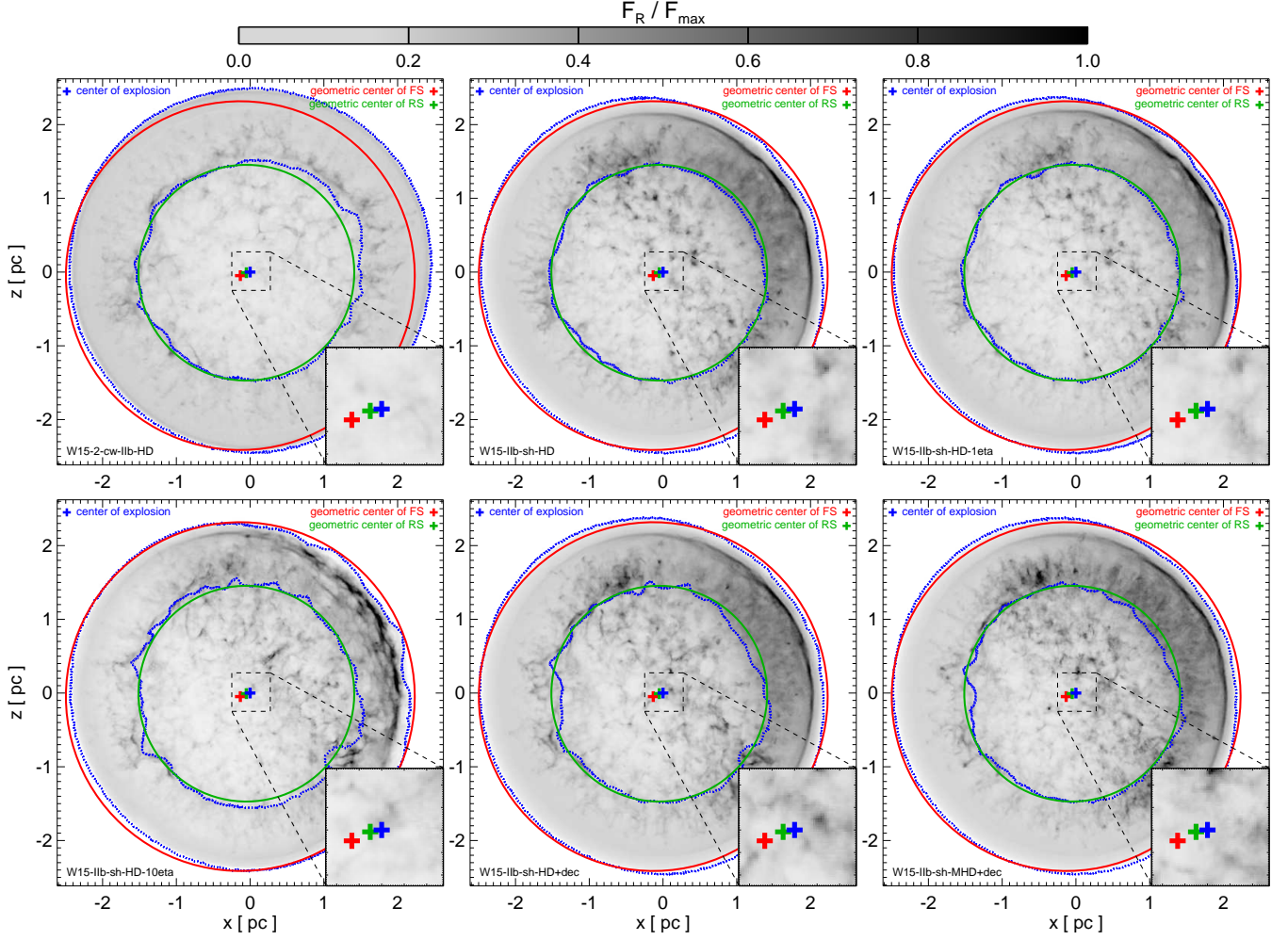


FIG. 7: Velocity of ejecta when they enter the reverse shock versus the position angle at the age of Cas A for the first six SNR models listed in Table 1, including model W15-2-cw-I Ib-HD presented in Paper I.

ejecta must be well above the limit for producing this emission ( $\approx 3000 \text{ km s}^{-1}$ ; Vink 2020). This may explain why most of the X-ray synchrotron emission originates from the western part of the reverse shock (Helder & Vink 2008) where the radio and X-ray observations agree on the position of the reverse shock (Vink 2020; see also Fig. 1). Interestingly, from the analysis of the 1 Ms Chandra observation of Cas A, Helder & Vink (2008) concluded that the dominant X-ray synchrotron emission from the western side of Cas A can be justified by a local reverse shock velocity in the ejecta frame of  $\approx 6000 \text{ km s}^{-1}$  as opposed to a velocity  $\approx 2000 \text{ km s}^{-1}$  elsewhere. Our models predict similar velocities.

The remnant-shell interaction can also alter the geometric centers of the forward and reverse shocks. Since these shocks can be easily traced by the nonthermal emission due to particle acceleration at the shock fronts (e.g., Arias et al. 2018), we synthesized the radio emission from the models at the age of Cas A. The synthesis has been performed using REMLIGHT, a code for the synthesis of synchrotron radio, X-ray, and inverse Compton  $\gamma$ -ray emission from MHD simulations (Orlando et al. 2007, 2011). Note that most of our simulations do not include an ambient magnetic field. In these cases we synthesized the non-thermal emission assuming a uniform randomized magnetic field with strength  $1 \mu\text{G}$  in the whole spatial domain. In model W15-I Ib-sh-MHD+dec, in which the ambient magnetic field configuration is described by the ‘‘Parker spiral’’ (Parker 1958), we synthesized the emission by adding a background uniform randomized magnetic field with strength  $0.5 \mu\text{G}$  to the spiral-shaped magnetic field; this was necessary to prevent a field strength very low at a distance of a few pc from the center of explosion and to make the field strength comparable to that assumed for the other models. We note that non-linear amplification of the field in proximity of the shock due to cosmic rays streaming instability is expected at the forward shock (Bell 2004) and, most likely, the same process is also operating at the reverse shock. Our models, however, do not include this effect. Hence our synthetic maps cannot be directly compared with radio observations of Cas A. In fact, as mentioned in Sect. 2.1, the radio emission was synthesized as a proxy of the position of the reverse shock, which is not expected to depend on the configuration and strength of the

<sup>5</sup> As mentioned in Sect. 3.2, simulations with  $r_{\text{sh}} > 1.5 \text{ pc}$  (not reported here) produce profiles of the forward shock velocity versus the position angle in the plane of the sky with a significant decrease in the NW side at odds with observations.



**Fig. 8:** Radio maps at the age of Cas A synthesized from the first six SNR models listed in Table 1, including model W15-2-cw-I Ib-HD (presented in Paper I). The maps are normalized to the maximum radio flux,  $F_{\max}$ , in model W15-I Ib-sh-HD-10eta. The blue dotted contours show cuts of the forward and reverse shocks in the plane of the sky passing through the center of the explosion (marked with a blue cross in each panel). The red and green circles mark the same cuts but for spheres roughly delineating the forward and reverse shocks, respectively, in models describing the remnant-shell interaction (the circles are the same in all the panels); the center of these spheres are marked with a cross of the same color (red or green) in each panel. These crosses represent the geometric center of the forward and reverse shocks, respectively, offset to the SE from the center of the explosion. The inset in the lower right corner of each panel is a zoom of the center of the domain.

magnetic field. On the other hand, we expect that higher reverse-shock strengths may produce higher magnetic field strengths and this may enhance the synchrotron emissivity in the NW side.

Fig. 8 shows the radio maps synthesized for the first six SNR models listed in Table 1. To better identify the effects of the remnant-shell interaction on the structure of the forward and reverse shocks, we compared the synthetic maps from these models with the radio map synthesized from model W15-2-cw-I Ib-HD (upper left panel in the figure). For each model, we derived the position of the forward and reverse shocks in the plane of the sky (blue contours in the figure) and fitted these positions (the contours) with circles (thus deriving the geometric centers and the radii of the forward and reverse shocks). We found that the centers and radii of the circles fitting the forward and reverse shocks are very similar in models which describe the remnant-shell interaction in Table 1. For this reason, the circles reported in Fig. 8 (red for the forward shock and green for the reverse shock) correspond to those derived from the fitting of the blue contours in model W15-I Ib-sh-HD-10eta and are the same in all

the panels to help in the comparison between model W15-2-cw-I Ib-HD and all the other models.

As expected the effects of the remnant-shell interaction are most evident in the NW region, where the shell has the highest density. In this region, both the forward and reverse shocks in models including the shell are at smaller radii from the center of the explosion than in model W15-2-cw-I Ib-HD. This is evident from the upper left panel in Fig. 8 where both the forward and reverse shocks in model W15-2-cw-I Ib-HD (blue contours) expand to NW more than in the other models (red and green circles). The forward shock slows down significantly as it propagates through the densest portion of the shell, bringing the shock front at a smaller distance from the center of the explosion than in model W15-2-cw-I Ib-HD. After the interaction with the shell, the forward shock starts propagating again with the same velocity as in model W15-2-cw-I Ib-HD (see Fig. 6) but with a smaller radius. As for the reverse shock, it interacts with the reflected shock from the shell which causes it to move inward in the observer frame in the NW region. As a result, in models in-

cluding the shell, also the reverse shock is at smaller radii from the center of the explosion than in model W15-2-cw-IIb-HD.

The asymmetry introduced by the interaction of the remnant with the shell leads to the geometric centers of the forward and reverse shocks (red and green crosses, respectively, in each panel of Fig. 8) that are shifted to the SE from the center of the explosion (blue cross in the figure). This is opposite to the result found in Paper I, where we found an offset of the geometric centers of the two shocks toward the NW by  $\approx 0.13$  pc from the center of the explosion. In fact, in models not including the interaction with the shell, the offset is caused by the initial asymmetric explosion, in which most of the  $^{56}\text{Ni}$  and  $^{44}\text{Ti}$  were ejected in the northern hemisphere away from the observer. Therefore, in our models, the effects of the remnant-shell interaction are opposite to those of the asymmetric explosion and dominate in the structure of the forward and reverse shocks at the age of Cas A.

Fig. 8 also shows that, at the age of Cas A, the forward shock appears more affected than the reverse shock by the remnant-shell interaction. We note that, while the forward shock passed through the shell at  $t \approx 180$  years after the SN, the reverse shock started to be affected by the reflected shock from the shell at later times, namely at  $t \approx 250 - 290$  years (see Sect. 3.1). This delay caused the distance between the reverse and forward shock to gradually decrease in the time interval between 180 and 250 years; then the distance started to increase for  $t > 250$  years when the reflected shock started to push the reverse shock inward. At the age of Cas A, the distance between the forward and reverse shocks in the NW region is still smaller than expected without the interaction with the shell.

An important consequence of the asymmetry introduced by the remnant-shell interaction is that, at the age of Cas A, the geometric center of the reverse shock is offset to the NW by  $\approx 0.1$  pc from the geometric center of the forward shock (the values range between 0.09 pc and 0.1 pc for the different models of remnant-shell interaction). This result differs from that of Paper I in which the geometric centers of the two shocks coincide. We note that the offset between the two shocks caused by the remnant-shell interaction is similar to that inferred from Cas A observations: the latter suggest that the reverse shock is offset to the NW by  $\approx 0.2$  pc (assuming a distance of 3.4 kpc) from the geometric center of the forward shock (e.g., Gotthelf et al. 2001). We note, however, that the shocks observed in Cas A deviate substantially from spherical shape. In fact the geometric centers of the two shocks were derived from azimuthal averages of the shock positions as inferred from observations and uncertainties can be of the order of 10 arcsec (i.e., 0.16 pc). Thus, we considered the direction of the offset as the main feature in discerning between models. While the difference in the values of the offset derived from observations and from the models may not be quantitatively significant given the uncertainties of fitting the shock locations with perfect circles, it is encouraging that the offset predicted by our models is consistent in extent and direction with that inferred from observations within the uncertainties.

It is worth mentioning that models producing, at the age of Cas A, an inward-moving reverse shock in the southern and western hemispheres (as suggested, e.g., by Sato et al. 2018) predict an offset to the south-west (SW) instead of NW, at odds with the observations of Cas A (see Appendix A). Given the idealized and simplified description of the asymmetric shell considered in our models, the offset develops along the direction between the center of the explosion and the densest side of the shell. Consequently, it always points to the region characterized by the inward motion of the reverse shock. Interestingly, this is not the case for Cas A, where the offset points to the NW and

inward-moving shocks are observed in the southern and western hemispheres (see Sato et al. 2018). The effects qualitatively shown here for the NW quadrant might operate as well in response to smaller-scale density enhancements in other directions; for instance, an interaction of the remnant with multiple shells or a more complex structure of the asymmetric shell may justify the observed asymmetries.

Finally, we note in Fig. 8 that the surface brightness of the radio emission is the highest in the NW region. This is due to two factors: i) the post-shock plasma having the highest density in this region as a result of the densest portion of the shell being shocked and ii) the highest velocity of the reverse shock in the ejecta rest frame (see Fig. 7). In model W15-IIb-sh-MHD+dec, the compression of the magnetic field in the interaction of the remnant with the shell further enhances the radio emission in the NW region (see lower right panel in Fig. 8). We stress again that a few words of caution are needed when comparing the radio maps derived here to actual radio observations of Cas A (as, for instance, the upper panel of Fig. 1): in fact, the synthesis of radio emission from the models does not take into account some relevant aspects such as the unknown nature of the ambient magnetic field configuration and its strength and the non-linear amplification of the field in proximity of the shocks due to cosmic rays streaming instability (Bell 2004). In fact, our synthetic radio maps show substantial differences with actual radio images of Cas A (compare, for instance, Fig. 8 with the upper panel of Fig. 1). Nevertheless, these maps are useful for identifying large-scale reverse shock asymmetries caused by the remnant-shell interaction. For instance, they predict a higher radio emission in the western than in the eastern hemisphere of the remnant as a consequence of the remnant-shell interaction, consistently with radio observations.

### 3.4. Effects of the shell on the Doppler velocity reconstruction

The excellent quality of the data collected for Cas A has allowed some authors to perform a very accurate 3D Doppler velocity reconstruction (Reed et al. 1995; DeLaney et al. 2010; Milisavljevic & Fesen 2013) to identify possible large-scale asymmetries of the remnant. The analysis of observed isolated knots of ejecta showed a significant blue and redshift velocity asymmetry: the ejecta traveling toward the observer (blueshifted) have, on average, lower velocities than ejecta traveling away (redshifted). As a result, the center of expansion of ejecta knots<sup>6</sup> appears to be redshifted with velocity  $v_c = 760 \pm 100 \text{ km s}^{-1}$  (Milisavljevic & Fesen 2013). The question is whether this asymmetry is due to the explosion dynamics (claimed by DeLaney et al. 2010; Isensee et al. 2010) or to the expansion of the remnant in inhomogeneous CSM (as suggested by Reed et al. 1995; Milisavljevic & Fesen 2013), possibly the circumstellar shell investigated in the present paper.

Our simulations include both the effects of the initial large-scale asymmetries inherited from the early phases of the SN explosion and the effects of interaction of the remnant with an asymmetric circumstellar shell. They therefore allow us to investigate the possible causes of the redshift measured for the center of expansion. From the simulations we can easily decompose the velocity of ejecta in each cell of the spatial domain into the component projected into the plane of the sky and the component

<sup>6</sup> All ejecta knots appear to lie on a spherical shell traveling radially outward from a unique center of expansion (e.g., Milisavljevic & Fesen 2013).

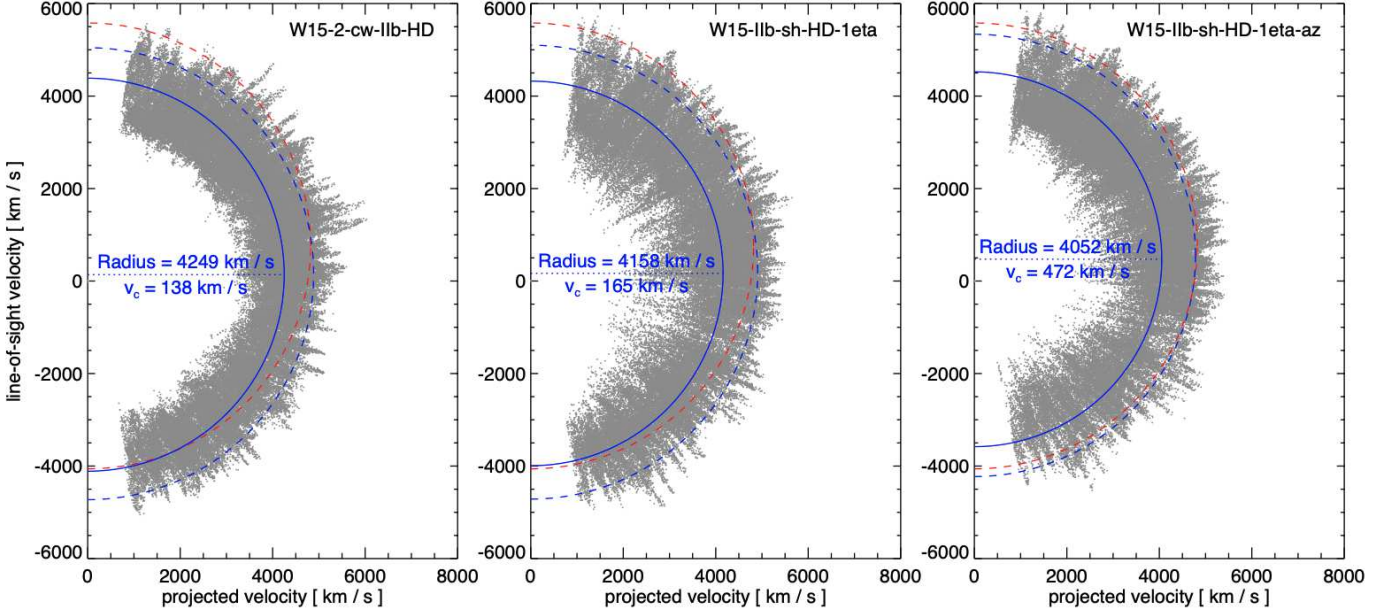


**FIG. 9:** Projected (in the plane of the sky) and LoS velocities at the age of Cas A derived from models W15-2-cw-IIb-HD (left panel), W15-IIb-sh-HD-1eta (center panel) and W15-IIb-sh-HD-1eta-az (right panel). The solid blue line in each panel is the best-fit semicircle to the data from the models; the dashed blue line shows the semicircle but artificially scaling the velocities to match the value of  $v_R$  inferred from Cas A observations; the dashed red line is the best-fit semicircle to actual data of Cas A derived by Milisavljevic & Fesen (2013).

along the LoS. The first is the analog of the projected velocity of isolated ejecta knots derived from their projected radii from the center of expansion in Cas A images and the second is the analog of the Doppler velocities of the same knots measured from the spectra of Cas A (e.g., Milisavljevic & Fesen 2013). For the analysis, we selected only cells composed of at least 90% of shocked ejecta. Hence, for each  $x$  and  $z$  coordinates, we have considered the cell with the highest kinetic energy along  $y$  (i.e., along the LoS). In other words, we selected cells characterized by a high mass of shocked ejecta and a significant velocity.

We first checked the apparent Doppler shift of the center of expansion introduced by the initial asymmetric SN explosion. To this end, we considered model W15-2-cw-IIb-HD, i.e. the case of a remnant that expands through the spherically symmetric wind of the progenitor star without any interaction with a circumstellar shell. The left panel of Fig. 9 shows the LoS velocities versus the projected velocities derived for this case. We fitted the data points of the scatter plot with a semicircle and found that the center of expansion is redshifted with velocity  $v_c = 138 \text{ km s}^{-1}$ . This redshift reflects the initial asymmetry of the SN explosion, resulting in a high concentration of  $^{44}\text{Ti}$  and  $^{56}\text{Ni}$  in the northern hemisphere, opposite to the direction of the kick velocity of the compact object (a neutron star) pointing south toward the observer (see Wongwathanarat et al. 2017). The radius of our best-fit semicircle corresponds to a velocity  $v_R = 4249 \text{ km s}^{-1}$ , lower than that found by Milisavljevic & Fesen (2013) from the analysis of observations ( $v_R = 4820 \text{ km s}^{-1}$ ). In fact, the explosion energy of our SN model ( $E_{\text{exp}} \approx 1.5 \text{ B}$ ; see Table 1) is a factor  $\approx 1.33$  smaller than the value inferred from the observations of Cas A,  $E_{\text{exp}} \approx 2 \text{ B}$  (e.g., Laming & Hwang 2003; Hwang & Laming 2003; Sato et al. 2020). If we consider that the explosion energy was almost entirely the kinetic energy of the ejecta, it is not surprising that the ejecta velocities in our models are smaller than the velocities observed in Cas A. However, even by artificially scaling the velocity of the model to match

the value of  $v_R$  found in Cas A, the value of  $v_c$  is much lower than that observed. In other words, an initial SN explosion with a large-scale asymmetry, which is capable of producing a distribution of  $^{44}\text{Ti}$  and  $^{56}\text{Ni}$  compatible with observations, leads to a redshift of the center of expansion significantly lower than that observed in Cas A (compare the dashed blue and red semicircles in the left panel of Fig. 9).

Then, we investigated whether an asymmetric shell as that discussed in this paper can account for the observed redshift of the center of expansion. The center panel of Fig. 9 shows the result for our reference model W15-IIb-sh-HD-1eta in which the remnant interacts with an asymmetric circumstellar shell with the symmetry axis perpendicular to the LoS (hence lying in the plane of the sky;  $\phi = 0$  in Eq. 1). We found that, in this case, the values of  $v_R$  and  $v_c$  are similar to those found with model W15-2-cw-IIb-HD. Thus, the interaction of the remnant with a shell that is symmetric with respect to the plane of the sky cannot contribute to determine the blue and redshift velocity asymmetry observed in Cas A. This was expected because, in this case, the effects of the shell on the propagation of ejecta are roughly the same in the blue and redshifted hemispheres of the remnant.

On the other hand, a denser shell on the blueshifted near-side would inhibit the forward expansion of ejecta toward the observer, resulting in an apparently redshifted center of expansion (Reed et al. 1995). To test this possibility, we ran further simulations similar to model W15-IIb-sh-HD-1eta but with the asymmetric shell oriented in such a way that its symmetry axis has an angle  $\phi > 0$  with respect to the plane of the sky. The right panel of Fig. 9 shows the results for our favorite model W15-IIb-sh-HD-1eta-az (see Table 1) in which the shell is similar to that adopted in model W15-IIb-sh-HD-1eta but rotated by  $50^\circ$  about the  $z$  axis, counterclockwise from the  $[x, z]$  plane (so that the densest portion of the shell is located in the nearside to the NW) and with a reference density  $n_{\text{sh}} = 20 \text{ cm}^{-3}$  (leading to a total mass of the shell of the order of  $M_{\text{sh}} \approx 2 M_\odot$ ; see param-

eters in Table 2). Increasing the reference density,  $n_{\text{sh}}$ , with respect to the models discussed in previous sections was necessary to keep shell densities in the western and southern sides of the  $[x, z]$  plane similar to those in model W15-IIb-sh-HD-1eta and, therefore, to produce profiles of forward and reverse shock velocities as those shown in Fig. 6 (see the upper panel of Fig. 10) and an offset between reverse and forward shocks of  $\approx 0.1$  pc to the NW, similar to those found in Fig. 8 (see lower panel of Fig. 10). With this shell configuration, the center of expansion appears to be redshifted with velocity  $v_c = 472$  km s $^{-1}$ . In this case, an artificial scaling of the modeled velocity which matches the observed value of  $v_R$  leads to a value of  $v_c$  much closer to that inferred from observations than in the other models, as is evident from the comparison of the dashed blue and red semicircles in the right panel of Fig. 9.

By comparing the lower panel of Fig. 10 with Fig. 8, we note that model W15-IIb-sh-HD-1eta-az is characterized by a significantly higher radio emission in the NW quadrant than the other models. This is the result of the density of the shocked shell, which is a factor of 2 higher than in the other models. Hence, an accurate analysis of the radio emission in the western hemisphere of Cas A may help constraining the density (and estimate the mass) of the putative circumstellar shell.

We conclude that the initial asymmetry in the SN explosion of Cas A determines a redshift in the center of expansion which, however, is not sufficient to justify the value inferred from the observations. The encounter of the remnant with a dense circumstellar shell leads to a further blue and redshift velocity asymmetry which makes the apparent redshift of the center of expansion compatible with the observations, if the nearside of the shell is denser than its opposite side. The scenario where Cas A interacted with an asymmetric circumstellar shell about a hundred years ago is also supported by the evidence that the majority of QSFs (76%) have blueshifted velocities (Reed et al. 1995), implying that there is more CSM material in the front than in the back. This provides additional reasons to suspect that the asymmetries associated with the reverse shock in Cas A can be attributed to inhomogeneities in the surrounding material.

#### 4. Summary and conclusions

In this work we investigated if some of the large-scale asymmetries observed in the reverse shock of Cas A (in particular, the inward-moving reverse shock observed in the western hemisphere of the remnant; Vink et al. 2022) can be interpreted as signatures of a past interaction of the remnant with a massive circumstellar shell, which is possibly a consequence of an episodic mass loss from the progenitor star that occurred in the latest phases of its evolution before collapse. To this end, we performed 3D HD and MHD simulations which describe the interaction of a SNR with an asymmetric dense shell of CSM. The SNR models are adapted from those presented in Paper I, which describe the formation of the remnant of a neutrino-driven SN explosion with asymmetries and features consistent with those observed in the ejecta distribution of Cas A.

The simulations follow the evolution from the breakout of the shock wave at the stellar surface ( $\approx 20$  hours after core-collapse) to the expansion of the remnant up to an age of  $\approx 2000$  yr. The initial conditions are provided by the output of a 3D neutrino-driven SN simulation that produces an ejecta distribution characterized by a large-scale asymmetry consistent with basic properties of Cas A (Wongwathanarat et al. 2017). The interaction of the remnant with the shell is assumed to occur during the first  $\approx 300$  years of evolution, namely at an epoch prior

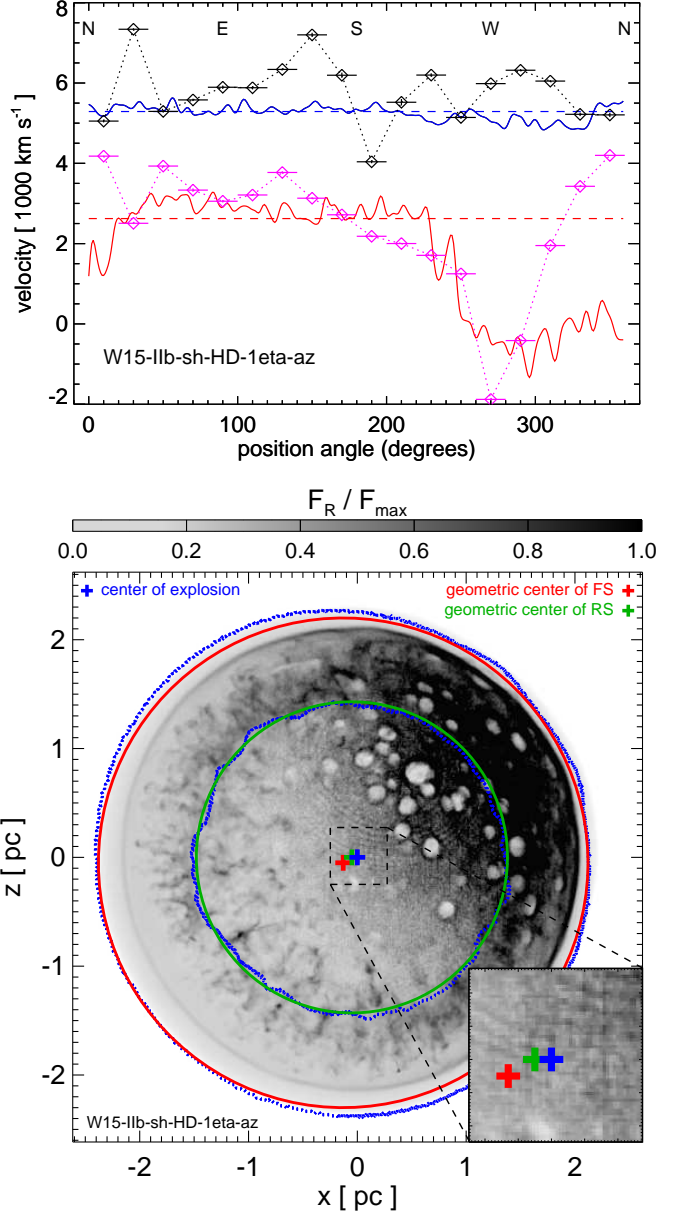


Fig. 10: Same as in Fig. 6 (upper panel) and in Fig. 8 (lower panel), but for model W15-IIb-sh-HD-1eta-az.

to the age of Cas A. We explored whether back-reaction of accelerated cosmic rays, energy deposition from radioactive decay or an ambient magnetic field (in the absence of nonlinear amplification) have a significant effect during the remnant-shell interaction by comparing models calculated with these physical processes turned either on or off. The model results at a remnant age of  $\approx 350 - 370$  yr were compared with the observations of Cas A.

More specifically, we explored the parameter space of the shell properties searching for a set of parameters (thickness, radius and total mass of the shell, density contrast between the two sides of the shell, orientation of the asymmetrical shell in the 3D space) which is able to produce profiles of forward and reverse shock velocities versus the position angle in the plane of the sky

similar to those observed in Cas A (Vink et al. 2022). The analysis of the simulations indicates the following.

- Initially the interaction of the remnant with the thin dense shell slows down the forward shock (because of its propagation through the denser medium of the shell) and drives a reflected shock, which propagates inward and interacts with the reverse shock. In case of an asymmetric shell with a side denser than the other, the effects of the interaction are the largest where the shell is the densest.
- After the forward shock crosses the shell, it propagates again through the  $r^{-2}$  density distribution of the stellar wind with velocities similar to those observed in models not including the shell. In contrast, the reverse shock is highly affected by the reflected shock from the shell and, depending on the shell density, the reverse shock can start moving inward in the observer frame, at odds with models not including the shell. We found that the signatures of the past interaction of the remnant with a thin dense shell of CSM persist in the reverse shock for a much longer time (at least for  $\approx 2000$  years in our models) than in the forward shock (just a few tens of years).
- Among the models analyzed, those producing reverse shock asymmetries analogous to those observed in Cas A predict that the shell was thin ( $\sigma \approx 0.02$  pc), with a radius  $r_{\text{sh}} \approx 1.5$  pc from the center of the explosion and that it was asymmetric with the densest portion in the nearside to the NW (model W15-IIb-sh-HD-1eta-az in Table 1).
- In the models listed in Table 1, the remnant-shell interaction determines the following asymmetries at the age of Cas A: i) the reverse shock moves inward in the observer frame in the NW region, while it moves outward in other regions; ii) the geometric center of the reverse shock is offset to the NW by  $\approx 0.1$  pc from the geometric center of the forward shock and both are offset to the SE from the center of the explosion; iii) significant nonthermal emission is expected from the reverse shock in the NW region because there the ejecta enter the reverse shock with a higher relative velocity (between 4000 and 7000 km s<sup>-1</sup>) than in other regions (below 2000 km s<sup>-1</sup>).
- The interaction of the remnant with a dense circumstellar shell can help explain the origin of the 3D asymmetry measured by Doppler velocities (e.g., Reed et al. 1995; DeLaney et al. 2010; Milisavljevic & Fesen 2013). We found that the asymmetry of the initial explosion, which is capable of producing distributions of <sup>44</sup>Ti and <sup>56</sup>Ni remarkably similar to those observed, leads to a redshifted center of expansion with velocity much lower than that observed. On the other hand, the interaction of the remnant with a shell which is denser in the (blueshifted) nearside than in the (redshifted) farside inhibits more the forward expansion of ejecta toward the observer, thus resulting in a center of expansion apparently redshifted with a velocity similar to that inferred from observations.
- The parameters of the shell do not change significantly if the back-reaction of accelerated cosmic rays, the energy deposition from radioactive decay or an ambient magnetic field are taken into account, although we have adopted a simplified modeling of these processes.

We emphasize that the primary aim of our study was to investigate whether the inward-moving reverse shock observed in the western hemisphere of Cas A may be the signature of a past interaction with a circumstellar shell. Though our study does not aim at deriving a unique and accurate reconstruction of the pre-SN circumstellar shell, it clearly demonstrates that the main

large-scale asymmetries observed in the reverse shock of Cas A can be interpreted as evidence that the remnant interacted with a thin shell of material, most likely ejected from the progenitor star before core-collapse. According to our study, the shell was not spherically symmetric but had one side denser than the other oriented to the NW and rotated by  $\approx 50^\circ$  toward the observer. This caused the main large-scale asymmetries now observed in the reverse shock of Cas A. We note that the remnant-shell interaction could also explain the different structure of the western jet compared to the eastern one, with the former less prominent and more jagged than the latter. Indeed this difference may indicate some interaction of the western jet with a dense CSM (maybe the circumstellar shell originated from the WR phase of the progenitor star, as suggested by Schure et al. 2008), at odds with the eastern jet which was free to expand through a less dense environment.

According to our favorite scenario, the shell was the result of a massive eruption that occurred between  $\approx 10^4$  and  $10^5$  years before the core-collapse, if we consider that the shell material was ejected, respectively, either at a few  $10^2$  km s<sup>-1</sup> (i.e., during an hypothetical common-envelope phase of the progenitor binary system) or at  $10 - 20$  km s<sup>-1</sup> (namely during the red supergiant phase of the progenitor<sup>7</sup>). Then the remnant started to interact with the shell  $\approx 180$  years after the SN explosion, when the shell had an average radius of 1.5 pc. Some authors have found that a hypothetical WR phase for the progenitor of Cas A may have lasted no more than a few thousand years, leading to a shell not larger than 1 pc (e.g., Schure et al. 2008; van Veelen et al. 2009). Our estimated radius of the shell (1.5 pc) and the presumed epoch of mass eruption (about  $10^4 - 10^5$  years before the SN), therefore, suggest that the shell has originated well before the WR phase (if any) of the progenitor of Cas A.

From our simulations, we have estimated a total mass of the shell of the order of  $M_{\text{sh}} \approx 2 M_\odot$  (see Sect. 3.4). Considering that the progenitor of Cas A was probably a star with a main sequence mass between 15 and 20  $M_\odot$  (according to the values suggested, e.g., by Aldering et al. 1994; Lee et al. 2014) and that the mass of the star before collapse was  $\approx 6 M_\odot$  (Nomoto et al. 1993), we expect a total mass lost during the latest phases of evolution of the progenitor to be between 9 and 14  $M_\odot$ . The estimated amount of mass of the shocked wind within the radius of the forward shock (assuming a spherically symmetric wind with gas density proportional to  $r^{-2}$ ) is  $\approx 6 M_\odot$  (see Orlando et al. 2016). Thus, including the shell, the mass of shocked CSM is  $\approx 8 M_\odot$ , so we can infer that less than 5  $M_\odot$  of CSM material is still outside the forward shock. We note that the mass of shocked CSM derived from our models is consistent with that inferred from the analysis of X-ray observations of Cas A (Borkowski et al. 1996; Lee et al. 2014).

It is worth to mention that the earliest radio images of Cas A collected in 1962 (i.e., when the remnant was  $\approx 310$  years old) already show a bright radio ring in which the western region is brighter than the eastern one (Ryle et al. 1965), indicating an increase in the synchrotron emissivity there over its value elsewhere in the ring, where our model predicts an increase in the reverse-shock strength. A stronger reverse shock could produce the asymmetry either through an increased efficiency of electron acceleration or through greater magnetic-field

<sup>7</sup> Note that the progenitor of Cas A was not a red supergiant at the time of core-collapse, namely after its outer H envelope was stripped away (e.g., Koo et al. 2020). At the same time, we cannot exclude that the progenitor was in the phase of red supergiant at the time of the mass eruption that produced the circumstellar shell.

amplification. This explanation requires that the encounter with an asymmetric shell must have taken place well before 1962. This is consistent with our models listed in Table 1 which predict that the remnant-shell interaction occurred between 180 and 240 years after the SN (i.e., between years 1830 and 1890) and that the reflected shock from the shell reached the reverse shock  $\approx 290$  years after the SN (i.e., in 1940). The observations collected in 1962, therefore, could witness the early inward propagation of the reverse shock in the western hemisphere.

Interestingly, the scenario supported by our models is consistent with that proposed by Koo et al. (2018) from the analysis of a long-exposure image centered at  $1.644 \mu\text{m}$  emission collected with the United Kingdom Infrared Telescope. From the analysis of the spatial distribution of QSFs, these authors have found a high concentration of these structures in the western hemisphere of Cas A and noted that their overall morphology is similar to that expected from a fragmented shell disrupted by fast-moving dense ejecta knots. Thus, they have interpreted the QSFs as the result of interaction of the remnant with an asymmetric shell of CSM. They have proposed that the progenitor system most likely ejected its envelope eruptively to the west about  $10^4 - 10^5$  years before the explosion (consistently with our findings). Koo et al. (2018) have estimated a total H+He mass of visible QSFs  $\approx 0.23 M_{\odot}$ ; considering a lifetime of QSFs  $\gtrsim 60$  yr, the mass can be a little larger ( $\approx 0.35 M_{\odot}$ ). The estimated mass of QSFs is lower than that estimated with our models (of the order of  $2 M_{\odot}$ ). However, if the QSFs are residuals of a shocked shell, they are certainly its densest component and a significant fraction of the shocked material from the shell may not be visible in the form of QSFs. Since the formation mechanism of the QSFs is still unknown, it is hard to estimate which fraction of the shell mass condensed to them. According to model W15-IIb-sh-HD-1eta-az, a shell mass of the order of  $2 M_{\odot}$  is strongly favored by the Doppler velocities discussed in Sect. 3.4, so that our conclusion here is that the mass determined for the QSFs can only be a small fraction of the total mass of the original shell. Our models show that the radio emission from the region of interaction of the remnant with the densest side of the shell is sensitive to the mass density of the shell. Thus, the analysis of radio emission may offer observational possibilities to better constrain the shell mass.

Although our models produce reverse shock asymmetries that qualitatively agree with the observations of Cas A, some issues still remain unexplained, for instance: i) the offset between the geometric centers of the reverse and forward shocks ( $\approx 0.1$  pc) is much smaller than that observed ( $\approx 0.2$  pc; Gotthelf et al. 2001); ii) in our models this offset points always to the region characterized by the inward motion of the reverse shock, whilst in Cas A the offset points to the NW but inward-moving shocks are also observed in the southern and western hemispheres. The discrepancies between models and observations might originate from the idealized and simplified description of the asymmetric shell adopted in the present study. For instance, observations have shown some density enhancements in the north-east region (Weil et al. 2020), where some evidence for deceleration of the forward shock was recently reported (Vink et al. 2022). These findings suggest that the CSM structure may be more complex than modeled here. It is plausible that a few mass eruptions at different epochs may have occurred before the collapse of the progenitor star, and each ejected shell of material may have had its own, generally non-spherical, structure. In this case, the more complex density structure of the circumstellar shell(s) may have induced large-scale asymmetries in the reverse shock that our models are unable to produce. Nevertheless, our

models naturally recover reverse shock asymmetries similar to those observed, thus supporting the scenario of interaction of the remnant with a circumstellar shell. A more accurate description of the CSM structure certainly require more observational input.

In the case of Cas A, several lines of evidence suggest that the progenitor star has experienced significant mass loss in its life time. For instance, from the analysis of XMM-Newton observations, Willingale et al. (2003) have estimated a total mass lost from the progenitor star before stellar death as high as  $\approx 20 M_{\odot}$  and suggested that the progenitor was a WR star that formed a dense nebular shell before collapse. In this respect, van Veelen et al. (2009) have performed HD simulations that describe the formation of the CSM around the progenitor of Cas A before the SN, considering several WR life times, and the subsequent expansion of the SNR through this CSM. Comparing the model results with observations, they have concluded that, most likely, the progenitor star of Cas A did not have a WR stage or that it lasted for less than a few thousands years (see also Schure et al. 2008). These authors, however, considered an almost spherically symmetric<sup>8</sup> cavity of the WR wind, so that, after interaction, the reverse shock was moving inward at all position angles. Thus, it still remains to investigate whether an asymmetric WR wind-cavity could have similar effects to those found here for the asymmetric shell. It is well possible that both these structures of the CSM contributed to determine the asymmetries observed in the reverse shock of Cas A.

Erratic mass-loss episodes are known to occur in massive stars before core-collapse. This is the case, for instance, of H-rich massive stars that are progenitors of SNe showing evidence of interaction with dense H- and/or He-rich CSM (hence of Type II<sub>n</sub> and/or Ib<sub>n</sub>, respectively), the result of mass-loss episodes occurred shortly before core-collapse (e.g., Smith et al. 2010; Fraser et al. 2013; Pastorello et al. 2013; Smith 2014; Ofek et al. 2014 and references therein). Large eruptions are observed in LBVs that, in fact, show large variations in both their spectra and brightness (e.g., Humphreys & Davidson 1994; Humphreys et al. 1999). In these cases, the dense and highly structured CSM in which the star explodes strongly influences the dynamics of the expanding remnant, which keeps memory of the interaction with the dense and structured CSM for hundreds of years after the SN (e.g., Ustamujic et al. 2021).

In recent years, observations have shown that H-poor progenitor stars can also experience significant mass-loss events before stellar death. Signs of interaction of the SN blast wave with a dense medium have been found in H-stripped Type-Ib<sub>n</sub> SNe (e.g., Foley et al. 2007; Pastorello et al. 2007), Type-IIb SNe (e.g., Gal-Yam et al. 2014; Maeda et al. 2015) and Type-Ib SNe (e.g., Svirski & Nakar 2014). Margutti et al. (2017) analyzed observations of SN 2014C during the first 500 days of evolution and found the signatures of the SN shock interaction with a dense shell of  $\approx 1 M_{\odot}$  at a distance of  $\approx 0.02$  pc, most likely the matter of a massive eruption from the progenitor in the decades before the collapse. Interestingly, the mass of the shell inferred from SN 2014C observations is similar (a factor of 2 lower) to that estimated here for the shell that interacted with Cas A (but, in the case of SN 2014C, the shell was ejected immediately before the collapse). The above examples indicate mass loss events occurred in the decades to centuries before collapse. Similar events could also have occurred in the hundreds of thousands of years before the SN, so that the remnant hits the

<sup>8</sup> The model includes HD instabilities which develop at the interaction front between the wind in the WR stage of the progenitor with the wind in the red supergiant stage (van Veelen et al. 2009).

relic of these mass eruptions even several hundreds of years after the explosion. For instance, observations of the Vela SNR have shown evidence of interaction of the remnant with a circumstellar shell with mass  $\approx 1.26 M_{\odot}$  (again similar to that found here) most likely blown by the progenitor star about  $10^6$  years before collapse (Sapienza et al. 2021).

If the scenario of a massive shell of material erupted by the progenitor of Cas A before collapse is confirmed, the information on the mass of the shell and time of the episodic mass loss can be useful to delineate the mass loss history of the progenitor star. This information may help to shed light on the question whether the progenitor of Cas A was a single star or a member in a binary and, more in general, whether the progenitor of Cas A (and of other Type-IIb SNe) might have lost its hydrogen envelope by an episode of interaction with a companion star in a binary system. Most likely the shell may be the result of one or multiple mass eruptions from the progenitor star during the late stages of star evolution (e.g., Smith et al. 2014; Levesque et al. 2014; Graham et al. 2014). However, it is interesting to note that shell asymmetries similar to that adopted here can also be produced by simulations describing the CSM of runaway massive stars in which lopsided bow shock nebulae result from the wind-ISM interaction (e.g., Meyer et al. 2017, 2020, 2021). These stars, moving supersonically through the ISM, can originate from the break-up of binary systems following the SN explosion of one of the binary components (e.g., Blaauw 1961; Stone 1991; Hoogerwerf et al. 2001; Dinçel et al. 2015) or as a consequence of dynamical multi-body encounters in dense stellar systems (e.g., Gies & Bolton 1986; Lada & Lada 2003; Gvaramadze & Gualandris 2011). Ascertain the interaction of Cas A with an asymmetric circumstellar shell reminiscent of those observed in runaway massive stars may help understanding the reason why the Cas A progenitor was stripped. Addressing the above issues may certainly be relevant to shed some light on the still uncertain physical mechanisms that drive mass loss in massive stars (e.g., Smith 2014). This is of pivotal importance given the role played by mass loss from massive stars in the galactic ecosystem, through its influence on the life time, luminosity and final fate of stars and its contribution on the chemical enrichment of the interstellar medium.

*Acknowledgements.* We thank the anonymous referee for the careful reading of the paper. The `pluto` code is developed at the Turin Astronomical Observatory (Italy) in collaboration with the Department of General Physics of Turin University (Italy) and the SCAI Department of CINECA (Italy). We acknowledge the CINECA ISCRA Award N.HP10BARP6Y for the availability of high performance computing (HPC) resources and support at the infrastructure Marconi based in Italy at CINECA. Additional computations were carried out on the HPC system MEUSA at the SCAN (Sistema di Calcolo per l’Astrofisica Numerica) facility for HPC at INAF-Osservatorio Astronomico di Palermo. Computer resources for this project have also been provided by the Max Planck Computing and Data Facility (MPCDF) on the HPC systems Cobra and Draco. S.O., M.M., F.B. and G.P. acknowledge financial contribution from the PRIN INAF 2019 grant “From massive stars to supernovae and supernova remnants: driving mass, energy and cosmic rays in our Galaxy” and the INAF mainstream program “Understanding particle acceleration in galactic sources in the CTA era”. At Garching, funding by the European Research Council through grant ERC-AdG no. 341157-COCO2CASA and by the Deutsche Forschungsgemeinschaft (DFG, German Research Foundation) through Sonderforschungsbereich (Collaborative Research Centre) SFB-1258 “Neutrinos and Dark Matter in Astro- and Particle Physics (NDM)” and under Germany’s Excellence Strategy through Cluster of Excellence ORIGINS (EXC-2094)-390783311 is acknowledged. S.N. and M.O. thank supports from JSPS KAKENHI Grant Numbers JP19H00693 and JP21K03545, respectively. S.N. and M.O. also thank supports from “Pioneering Program of RIKEN for Evolution of Matter in the Universe (r-EMU)” and “Interdisciplinary Theoretical and Mathematical Sciences Program of RIKEN”. The navigable 3D graphics have been developed in the framework of the project 3DMAP-VR (3-Dimensional Modeling of Astrophysical Phenomena in Virtual Reality; Orlando et al. 2019b) at INAF-Osservatorio Astronomico di Palermo.

## Appendix A: Alternative asymmetry of the circumstellar shell

The asymmetry of the circumstellar shell investigated in the main body of the paper leads to a reverse shock moving inward in the observer frame, in the NW hemisphere. This feature does not fit well with observations of Cas A that show inward-moving shocks preferentially in the western and southern hemispheres (e.g., Anderson & Rudnick 1995; Keohane et al. 1996; DeLaney et al. 2004; Helder & Vink 2008; Sato et al. 2018). A better match of the models with observations may be obtained by changing the orientation of the asymmetric shell. We considered, therefore, the setup of model W15-IIb-sh-HD-1eta and rotated the shell by approximately  $90^\circ$  clockwise about the  $y$  axis (model W15-IIb-sh-HD-1eta-sw). The upper panel in Fig. A.1 shows the forward and reverse shock velocities versus the position angle in the plane of the sky at the age of Cas A derived from the analysis of this model. As expected, in model W15-IIb-sh-HD-1eta-sw, the reverse shock moves inward in the western and southern hemispheres. We note, however, that, in this way, the model is able to roughly match the velocity profiles of forward and reverse shocks in the NW quadrant, but it fails in reproducing the profiles in the south-west quadrant (compare red and magenta curves in the upper panel of Fig. A.1).

Furthermore, we found that other asymmetries that characterize the remnant morphology are not reproduced by simply changing the orientation of the asymmetric shell. In particular, model W15-IIb-sh-HD-1eta-sw predicts an offset of  $\approx 0.1$  pc to the SW between the geometric center of the reverse shock and that of forward shock, at odds with observations that show an offset of  $\approx 0.2$  pc to the NW (e.g., Gotthelf et al. 2001). This is evident from the lower panel in Fig. A.1 that reports the radio map normalized to the maximum radio flux in model W15-IIb-sh-HD-1eta-sw. The blue dotted contours show cuts of the forward and reverse shocks in the plane of the sky passing through the center of the explosion (marked with a blue cross). The red and green circles mark the same cuts but for spheres roughly delineating the forward and reverse shocks in model W15-IIb-sh-HD-1eta-sw, respectively. The centers of these spheres (marked with a cross of the same color of the corresponding circles) represent the geometric centers of the forward and reverse shocks, respectively, that are offset to the north-east from the center of the explosion.

For the simple asymmetry considered for the circumstellar shell, we found that, in general, the offset between the geometric center of the reverse shock and that of forward shock points toward the densest portion of the shell where the reverse shock propagates inward in the observer frame. We concluded that an interaction with multiple shells or with a shell with a more complex structure and geometry may be required to better match the observations of Cas A.

## References

- Aldering, G., Humphreys, R. M., & Richmond, M. 1994, *AJ*, 107, 662
- Anderson, M. C. & Rudnick, L. 1995, *ApJ*, 441, 307
- Arias, M., Vink, J., de Gasperin, F., et al. 2018, *A&A*, 612, A110
- Bell, A. R. 2004, *MNRAS*, 353, 550
- Blaauw, A. 1961, *Bull. Astron. Inst. Netherlands*, 15, 265
- Blasi, P., Gabici, S., & Vannoni, G. 2005, *MNRAS*, 361, 907
- Borkowski, K., Szymkowiak, A. E., Blondin, J. M., & Sarazin, C. L. 1996, *ApJ*, 466, 866
- Chevalier, R. A., Blondin, J. M., & Emmering, R. T. 1992, *ApJ*, 392, 118
- Chevalier, R. A. & Kirshner, R. P. 1978, *ApJ*, 219, 931
- Chevalier, R. A. & Liang, E. P. 1989, *ApJ*, 344, 332

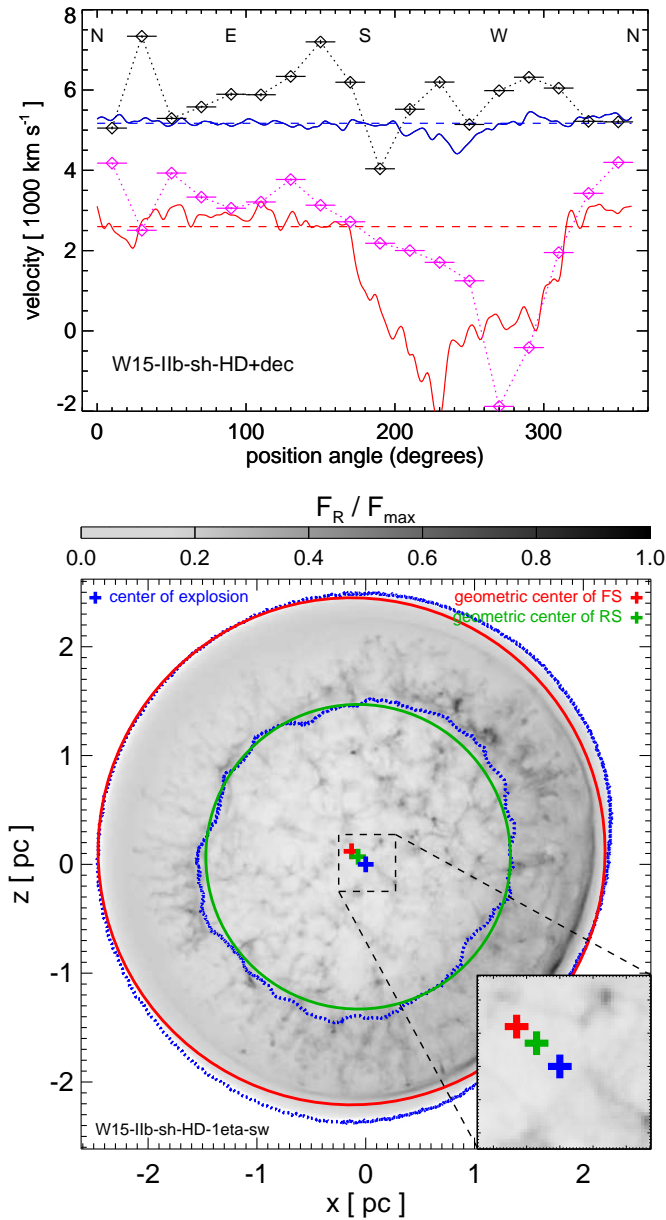


**FIG. A.1:** Same as in Fig. 6 (upper panel) and in Fig. 8 (lower panel), but for model W15-IIb-sh-HD-1eta-sw.

Conti, P. S. 1984, in *Observational Tests of the Stellar Evolution Theory*, ed. A. Maeder & A. Renzini, Vol. 105, 233  
 DeLaney, T. & Rudnick, L. 2003, *ApJ*, 589, 818  
 DeLaney, T., Rudnick, L., Fesen, R. A., et al. 2004, *ApJ*, 613, 343  
 DeLaney, T., Rudnick, L., Stage, M. D., et al. 2010, *ApJ*, 725, 2038  
 Dinçel, B., Neuhäuser, R., Yerli, S. K., et al. 2015, *MNRAS*, 448, 3196  
 Donati, J.-F. & Landstreet, J. D. 2009, *ARA&A*, 47, 333  
 Dunne, L., Maddox, S. J., Ivison, R. J., et al. 2009, *MNRAS*, 394, 1307  
 Ferrand, G., Warren, D. C., Ono, M., et al. 2019, *ApJ*, 877, 136  
 Fesen, R., Patnaude, D., Milisavljevic, D., Weil, K., & Brumback, M. 2019, in “Supernova Remnants: An Odyssey in Space after Stellar Death II”, invited talk, 3-8 June 2019, Chania, Crete, Greece, (online at <http://snr2019.astro.noa.gr/index.php/program>)  
 Fesen, R. A., Hammell, M. C., Morse, J., et al. 2006, *ApJ*, 645, 283  
 Foley, R. J., Smith, N., Ganeshalingam, M., et al. 2007, *ApJ*, 657, L105  
 Fraser, M., Magee, M., Kotak, R., et al. 2013, *ApJ*, 779, L8  
 Fryxell, B., Mueller, E., & Arnett, D. 1991, *ApJ*, 367, 619  
 Gal-Yam, A., Arcavi, I., Ofek, E. O., et al. 2014, *Nature*, 509, 471

Ghavamian, P., Laming, J. M., & Rakowski, C. E. 2007, *ApJ*, 654, L69  
 Giacalone, J. & Jokipii, J. R. 2007, *ApJ*, 663, L41  
 Gies, D. R. & Bolton, C. T. 1986, *ApJS*, 61, 419  
 Gotthelf, E. V., Koralesky, B., Rudnick, L., et al. 2001, *ApJ*, 552, L39  
 Graham, M. L., Sand, D. J., Valenti, S., et al. 2014, *ApJ*, 787, 163  
 Grefenstette, B. W., Fryer, C. L., Harrison, F. A., et al. 2017, *ApJ*, 834, 19  
 Grefenstette, B. W., Harrison, F. A., Boggs, S. E., et al. 2014, *Nature*, 506, 339  
 Gull, S. F. 1973, *MNRAS*, 161, 47  
 Gvaramadze, V. V. & Gualandris, A. 2011, *MNRAS*, 410, 304  
 Heger, A., Fryer, C. L., Woosley, S. E., Langer, N., & Hartmann, D. H. 2003, *ApJ*, 591, 288  
 Helder, E. A. & Vink, J. 2008, *ApJ*, 686, 1094  
 Hirai, R., Sato, T., Podsiadlowski, P., Vigna-Gómez, A., & Mandel, I. 2020, *MNRAS*, 499, 1154  
 Hoogerwerf, R., de Bruijne, J. H. J., & de Zeeuw, P. T. 2001, *A&A*, 365, 49  
 Humphreys, R. M. & Davidson, K. 1994, *PASP*, 106, 1025  
 Humphreys, R. M., Davidson, K., & Smith, N. 1999, *PASP*, 111, 1124  
 Hwang, U. & Laming, J. M. 2003, *ApJ*, 597, 362  
 Hwang, U. & Laming, J. M. 2012, *ApJ*, 746, 130  
 Inoue, T., Yamazaki, R., & Inutsuka, S.-i. 2009, *ApJ*, 695, 825  
 Isensee, K., Rudnick, L., DeLaney, T., et al. 2010, *ApJ*, 725, 2059  
 Jeffery, D. J. 1999, *arXiv:astro-ph/9907015*  
 Kamper, K. & van den Bergh, S. 1976, *ApJS*, 32, 351  
 Keohane, J. W., Rudnick, L., & Anderson, M. C. 1996, *ApJ*, 466, 309  
 Kilpatrick, C. D., Biegging, J. H., & Rieke, G. H. 2014, *ApJ*, 796, 144  
 Koo, B.-C., Kim, H.-J., Lee, Y.-H., et al. 2018, *ApJ*, 866, 139  
 Koo, B.-C., Kim, H.-J., Oh, H., et al. 2020, *Nature Astronomy*, 4, 584  
 Krause, O., Birkmann, S. M., Rieke, G. H., et al. 2004, *Nature*, 432, 596  
 Krause, O., Birkmann, S. M., Usuda, T., et al. 2008, *Science*, 320, 1195  
 Lada, C. J. & Lada, E. A. 2003, *ARA&A*, 41, 57  
 Laming, J. M. & Hwang, U. 2003, *ApJ*, 597, 347  
 Lee, J.-J., Park, S., Hughes, J. P., & Slane, P. O. 2014, *ApJ*, 789, 7  
 Levesque, E. M., Stringfellow, G. S., Ginsburg, A. G., Bally, J., & Keeney, B. A. 2014, *AJ*, 147, 23  
 Maeda, K., Hattori, T., Milisavljevic, D., et al. 2015, *ApJ*, 807, 35  
 Margutti, R., Kamble, A., Milisavljevic, D., et al. 2017, *ApJ*, 835, 140  
 Meyer, D. M. A., Mignone, A., Kuiper, R., Raga, A. C., & Kley, W. 2017, *MNRAS*, 464, 3229  
 Meyer, D. M. A., Mignone, A., Petrov, M., et al. 2021, *MNRAS*, 506, 5170  
 Meyer, D. M. A., Oskinova, L. M., Pohl, M., & Petrov, M. 2020, *MNRAS*, 496, 3906  
 Mignone, A., Bodo, G., Massaglia, S., et al. 2007, *ApJS*, 170, 228  
 Mignone, A., Zanni, C., Tzeferacos, P., et al. 2012, *ApJS*, 198, 7  
 Milisavljevic, D. & Fesen, R. A. 2013, *ApJ*, 772, 134  
 Milisavljevic, D. & Fesen, R. A. 2015, *Science*, 347, 526  
 Morse, J. A., Fesen, R. A., Chevalier, R. A., et al. 2004, *ApJ*, 614, 727  
 Nomoto, K., Suzuki, T., Shigeyama, T., et al. 1993, *Nature*, 364, 507  
 Ofek, E. O., Sullivan, M., Shaviv, N. J., et al. 2014, *ApJ*, 789, 104  
 Orlando, S., Bocchino, F., Miceli, M., Petruk, O., & Pumo, M. L. 2012, *ApJ*, 749, 156  
 Orlando, S., Bocchino, F., Reale, F., Peres, G., & Petruk, O. 2007, *A&A*, 470, 927  
 Orlando, S., Miceli, M., Petruk, O., et al. 2019a, *A&A*, 622, A73  
 Orlando, S., Miceli, M., Pumo, M. L., & Bocchino, F. 2015, *ApJ*, 810, 168  
 Orlando, S., Miceli, M., Pumo, M. L., & Bocchino, F. 2016, *ApJ*, 822, 22  
 Orlando, S., Petruk, O., Bocchino, F., & Miceli, M. 2011, *A&A*, 526, A129  
 Orlando, S., Pillitteri, I., Bocchino, F., Daricello, L., & Leonardi, L. 2019b, *Research Notes of the American Astronomical Society*, 3, 176  
 Orlando, S., Wongwathanarat, A., Janka, H. T., et al. 2021, *A&A*, 645, A66  
 Parker, E. N. 1958, *ApJ*, 128, 664  
 Pastorello, A., Cappellaro, E., Inger, C., et al. 2013, *ApJ*, 767, 1  
 Pastorello, A., Quimby, R. M., Smartt, S. J., et al. 2008, *MNRAS*, 389, 131  
 Pastorello, A., Smartt, S. J., Mattila, S., et al. 2007, *Nature*, 447, 829  
 Patnaude, D. J. & Fesen, R. A. 2009, *ApJ*, 697, 535  
 Podsiadlowski, P., Joss, P. C., & Hsu, J. J. L. 1992, *ApJ*, 391, 246  
 Reed, J. E., Hester, J. J., Fabian, A. C., & Winkler, P. F. 1995, *ApJ*, 440, 706  
 Rest, A., Foley, R. J., Sinnott, B., et al. 2011, *ApJ*, 732, 3  
 Ryle, M., Elsmore, B., & Neville, A. C. 1965, *Nature*, 205, 1259  
 Sanders, J. S. 2006, *MNRAS*, 371, 829  
 Sapienza, V., Miceli, M., Peres, G., et al. 2021, *A&A*, 649, A56  
 Sato, T., Katsuda, S., Morii, M., et al. 2018, *ApJ*, 853, 46  
 Sato, T., Yoshida, T., Umeda, H., et al. 2020, *ApJ*, 893, 49  
 Schure, K. M., Vink, J., García-Segura, G., & Achterberg, A. 2008, *ApJ*, 686, 399  
 Slane, P., Bykov, A., Ellison, D. C., Dubner, G., & Castro, D. 2015, *Space Sci. Rev.*, 188, 187  
 Smith, N. 2014, *ARA&A*, 52, 487  
 Smith, N., Chornock, R., Silverman, J. M., Filippenko, A. V., & Foley, R. J.

- 2010, *ApJ*, 709, 856
- Smith, N., E Andrews, J., Moe, M., et al. 2020, *MNRAS*, 492, 5897
- Smith, N., Mauerhan, J. C., & Prieto, J. L. 2014, *MNRAS*, 438, 1191
- Stone, R. C. 1991, *AJ*, 102, 333
- Svirski, G. & Nakar, E. 2014, *ApJ*, 788, L14
- Timmes, F. X. & Swesty, F. D. 2000, *ApJS*, 126, 501
- Ustamujic, S., Orlando, S., Miceli, M., et al. 2021, *A&A*, 654, A167
- van Veelen, B., Langer, N., Vink, J., García-Segura, G., & van Marle, A. J. 2009, *A&A*, 503, 495
- Vink, J. 2020, *Physics and Evolution of Supernova Remnants (Astronomy and Astrophysics Library (Cham: Springer International Publishing))*
- Vink, J., Patnaude, D. J., & Castro, D. 2022, *ApJ*, 929, 57
- Weil, K. E., Fesen, R. A., Patnaude, D. J., et al. 2020, *ApJ*, 891, 116
- Willingale, R., Bleeker, J. A. M., van der Heyden, K. J., & Kaastra, J. S. 2003, *A&A*, 398, 1021
- Willingale, R., Bleeker, J. A. M., van der Heyden, K. J., Kaastra, J. S., & Vink, J. 2002, *A&A*, 381, 1039
- Wilson, T. L. & Batrla, W. 2005, *A&A*, 430, 561
- Wongwathanarat, A., Janka, H. T., & Müller, E. 2013, *A&A*, 552, A126
- Wongwathanarat, A., Janka, H.-T., Müller, E., Pllumbi, E., & Wanajo, S. 2017, *ApJ*, 842, 13
- Wongwathanarat, A., Müller, E., & Janka, H.-T. 2015, *A&A*, 577, A48
- Woosley, S. E. & Weaver, T. A. 1995, *ApJS*, 101, 181